





# Efficient Calculation of Non-local Thermodynamic Equilibrium Effects in Multithreaded Hydrodynamic Simulations of Solar Flares

Jeffrey W. Reep<sup>1</sup> , Stephen J. Bradshaw<sup>2</sup>, Nicholas A. Crump<sup>1</sup>, and Harry P. Warren<sup>1</sup> 

<sup>1</sup>Space Science Division, Naval Research Laboratory, Washington, DC 20375, USA; [jeffrey.reep@nrl.navy.mil](mailto:jeffrey.reep@nrl.navy.mil)

<sup>2</sup>Department of Physics & Astronomy, Rice University, Houston, TX 77005, USA

Received 2018 June 7; revised 2018 November 5; accepted 2018 November 19; published 2019 January 18

## Abstract

Understanding the dynamics of the chromosphere is crucial to understanding energy transport across the solar atmosphere. The chromosphere is optically thick at many wavelengths and described by non-local thermodynamic equilibrium (NLTE), making it difficult to interpret observations. Furthermore, there is considerable evidence that the atmosphere is filamented, and that current instruments do not resolve small-scale features. In flares, it is likely that multithreaded models are required to describe the heating. The combination of NLTE effects and multithreaded modeling requires computationally demanding calculations, which has motivated the development of a model that can efficiently treat both. We describe the implementation of a solver in a hydrodynamic code for the hydrogen level populations that approximates the NLTE solutions. We derive an accurate electron density across the atmosphere that includes the effects of nonequilibrium ionization for helium and metals. We show the effects on hydrodynamic simulations, which are used to synthesize light curves using a postprocessing radiative transfer code. We demonstrate the utility of this model on *IRIS* observations of a small flare. We show that the Doppler shifts in Mg II, C II, and O I can be explained with a multithreaded model of loops subjected to electron beam heating, so long as NLTE effects are treated. The intensities, however, do not match the observed values very well, which is due to assumptions about the initial atmosphere. We briefly show how altering the initial atmosphere can drastically alter line profiles and derived quantities and suggest that it should be tuned to preflare observations.

**Key words:** Sun: atmosphere – Sun: chromosphere – Sun: corona – Sun: flares – Sun: transition region

**Supporting material:** animations

## 1. Introduction

The solar chromosphere and corona are intimately connected through the transport of mass, momentum, and energy. In order to understand the coronal response to solar flare heating events, a chromospheric model must be developed. The chromosphere, however, is not in local thermodynamic equilibrium (LTE); therefore, radiative processes cannot be ignored in general (Carlsson & Stein 2002). In order to calculate an accurate electron density, for example, one must determine the ionization fractions of the most abundant elements, which in turn requires knowledge of the radiation field. It is therefore crucial to deal with non-LTE (NLTE) and radiative transfer effects. The computational treatment of radiative transfer is a hugely demanding task, and the development of computational schemes remains an active field of research (e.g., Judge 2017).

To make matters worse, the solar atmosphere is generally filamented, meaning that there are many small-scale structures and features beneath the resolution of modern instrumentation. Substructuring of active region loops has been found when comparing AIA images to higher-resolution Hi-C data (e.g., Brooks et al. 2013), as well as in coronal rain when comparing AIA images to higher-resolution H $\alpha$  data (Antolin et al. 2015) and in flare spectral data with *IRIS* (Warren et al. 2016). These facts point to the necessity of multithreaded models to accurately capture the details of the emission and thus the underlying energy release and transport processes. We therefore wish to have a model that can capture multithreaded details of dynamic events while simultaneously treating NLTE effects in the chromosphere, both of which are computational challenges in their own right.

In this work, we describe the implementation of such a model. Using a hydrodynamic code, we have implemented an approximation to the radiative transfer equations in order to solve the hydrogen level populations in NLTE and thereby determine a more accurate electron density. We give full details of this implementation and examine an example simulation in detail. We then follow the methodology of our previous work to create a multithreaded model of a solar flare (Reep et al. 2016b), which we then contrast against observations of light curves and Doppler shifts.

Our comparison focuses on observations of a small flare by *IRIS* (De Pontieu et al. 2014), in which Warren et al. (2016) found redshifts in spectral lines that persisted for well over 30 minutes. Specifically, Si IV 1402.77 Å and C II 1334.54 Å were redshifted for long periods of time near the flare ribbon, while Mg II 2796.354 Å showed redshifts that gradually decayed. Similarly behaved redshifts are seen routinely in flares with *IRIS*, e.g., Graham & Cauzzi (2015), Li et al. (2015), Polito et al. (2016), Brosius & Inglis (2017), and Tian & Chen (2018); less commonly with the *Solar and Heliospheric Observatory*/CDS (Brosius & Phillips 2004); and possibly in He II 303.78 Å with *Hinode*/EIS (Lee et al. 2017, though that line has multiple blends with coronal iron lines). These observations are surprising in light of the results of Fisher (1989), who showed that chromospheric condensation events only last for about a minute, regardless of the strength or duration of the heating, which might sufficiently explain the Mg II emission but not the other lines. Although it was not explicitly shown in Warren et al. (2016), O I 1355.60 Å was essentially stationary (shown in Section 4 of this paper).

In order to explain the persistent redshifts, therefore, Reep et al. (2016b) used a multithreaded model where a large number of loops rooted within one *IRIS* pixel are successively heated, thereby causing successive condensation events and producing a long-lasting redshift. This model was consistent with the Si IV emission, though the C II line had a much stronger stationary component than the model. Furthermore, the model predicted that the O I line should be redshifted at around  $10 \text{ km s}^{-1}$ , in contradiction with the observations of a stationary line. One possible explanation is that the forward modeling erroneously assumed that the lines were optically thin, which may or may not hold true for C II (Rathore & Carlsson 2015) and O I (Lin & Carlsson 2015), depending on the particular conditions of the event. It is also possible that the line shapes may be non-Maxwellian, which can affect the opacity (Dudík et al. 2017). We seek to directly test the importance of NLTE effects by redoing the simulations with the improved model and then synthesizing the emission with a radiative transfer solver.

In this paper, we first describe the method in Section 2 that we implement to give an approximation to the level populations of hydrogen in the chromosphere, thereby improving the resultant electron density and better treating the effects of NLTE. We then examine the details of a loop subjected to heating by an electron beam in Section 3. Then, in Section 4, we use a multithreaded model of a beam-heated flare to forward model line profiles, light curves, and Doppler shifts in order to compare with observations. We show that many features are consistent with observations, but the assumed initial atmosphere can have a large impact on the results.

## 2. Implementation

In this section, we describe a method by which we solve the NLTE level populations and ionization state of hydrogen, which we have added to the field-aligned HYDrodynamics and RADiation code (HYDRAD; Bradshaw & Mason 2003a; Bradshaw & Cargill 2013). HYDRAD solves the equations describing the conservation of mass, momentum, and energy for a two-fluid plasma constrained to a magnetic flux tube. The code solves the full loop length in an arbitrary geometry in terms of loop shape, inclination, and expanding cross-section (equivalently, varying magnetic field strength). It includes the effects of full nonequilibrium ionization for any desired element, returning the ion populations and an accurate calculation of the radiative losses. HYDRAD also makes use of adaptive mesh refinement of arbitrary order, important for accurately resolving sharp gradients in density and temperature. The code is light enough to run on a desktop (tested on Linux, Mac, and Windows) but general enough to run on high-performance computing machines.

In previous versions, the chromospheric ionization fraction was calculated with LTE assumptions, i.e., that the ionization fraction is determined by the local density and temperature and that it is collisionally dominated. To improve upon this, we use the method for computing NLTE effects outlined in Leenaarts & Wedemeyer-Böhm (2006) and Leenaarts et al. (2007), which is in turn based on the method derived by Sollum (1999). For completeness, we reiterate many of the details from those works and note a few small points that differ from these other works (e.g., atomic parameters).

We wish to solve the level populations of the hydrogen atom with the equation

$$\frac{\partial n_i}{\partial t} + \frac{\partial}{\partial s}(n_i v) = \sum_{j \neq i} n_j P_{ji} - n_i \sum_{j \neq i} P_{ij}, \quad (1)$$

where  $n_i$  is the fractional level population of level  $i$  and  $v$  is the bulk flow velocity. The rate coefficient  $P_{ij}$  represents the rate ( $\text{s}^{-1}$ ) at which atoms transition from level  $i$  to level  $j$  (and vice versa for  $P_{ji}$ ). We solve this equation for a six-level hydrogen atom, including the first five levels (principal quantum number  $n$  from 1 to 5) plus the ionized state.

### 2.1. Rate Coefficients

The rate coefficients  $P_{ij}$  are the sum of the collisional and radiative rates:

$$P_{ij} = C_{ij} + R_{ij}. \quad (2)$$

The collisional rate coefficients  $C_{ij}$  are taken directly from the tables bundled with the RH1.5D code (Uitenbroek 2001; Pereira & Uitenbroek 2015), which in turn are based on Johnson (1972). They are lookup tables as a function of density and temperature, which we interpolate to calculate the local coefficients.

The radiative rate coefficients  $R_{ij}$  require a detailed calculation to accurately determine. In general, a full solution of the radiative transfer equations is necessary to determine the radiation field, which in turn determines the rates. In the RADYN code (Carlsson & Stein 1992; Allred et al. 2015), the transfer equation is solved with the method from Scharmer (1981) and Scharmer & Carlsson (1985), while the Flarix code (Heinzel et al. 2016) uses an accelerated  $\lambda$ -iteration method (Rybicki & Hummer 1991). In this work, we follow the prescription derived by Sollum (1999) that gives a method for approximating the radiation field in the chromosphere, which is somewhat less accurate than the methods used in RADYN or Flarix but significantly less computationally demanding. For similar reasons, the method is also implemented in the Bifrost MHD code (Gudiksen et al. 2011).

The prescription for the radiation field has a few key assumptions. First, it is assumed that below a certain height in the chromosphere, the population is in LTE. This can be due to either of two options: the collisional rates dominate the radiative rates or the radiation field is well-described by a Planck function, both of which are true at the photosphere and in the lower chromosphere. Below this critical height, therefore, the radiation field is assumed to be described by a Planck function.

Second, the Lyman transitions are assumed to be in detailed balance in the chromosphere (Carlsson & Stein 2002):  $n_i R_{ij} = n_j R_{ji}$ , which says that the number of transitions into the ground state from state  $j$  equals the number from the ground state into state  $j$ . This allows the simplification that the net rates for the Lyman transitions are collisionally dominated:  $P_{ij} \approx C_{ij}$ . Sollum (1999) tested this approximation in depth, finding that the errors are negligible in the chromosphere and become more significant in the transition region.

Third, it is assumed that the radiation field for each transition at a given location can be characterized by a local brightness temperature  $T_b$ , defined by Sollum (1999) as the temperature where the Planck function  $B_\nu(T_b)$  equals the intensity at that

wavelength,

$$J_\nu = \frac{2h\nu^3}{c^2} \frac{1}{\exp\left(\frac{h\nu}{k_B T_b}\right) - 1}, \quad (3)$$

where  $\nu$  is the frequency of the transition,  $h$  is Planck's constant,  $c$  is the speed of light, and  $k_B$  is the Boltzmann constant. The brightness temperature is not an actual temperature but rather a convenient parameter that characterizes the radiation field (as commonly done in radio astronomy). Note that Sollum (1999) and Leenaarts & Wedemeyer-Böhm (2006) refer to this temperature as the ‘‘radiation temperature’’ rather than the brightness temperature.

Finally, for each transition at each location and time, the brightness temperature must be determined. At the top of the chromosphere, the brightness temperature  $T_b^{\text{top}}$  is taken as input based on the Sollum (1999) study, which we list in the Appendix. Next, we determine a critical height  $z_{\text{crit}}$  for each transition defined as the lowest point in the atmosphere where  $J_\nu(T_e) = 2J_\nu(T_b^{\text{top}})$ , which for most transitions is near the temperature minimum region. Below this height, we assume  $T_b(z < z_{\text{crit}}) = T_e(z)$ , and above this height, the brightness temperature is a function of the column mass (equivalently, the optical depth),

$$J_\nu(z) = B_\nu(T_b^{\text{top}}) + [B_\nu(T_e(z_{\text{crit}})) - B_\nu(T_b^{\text{top}})] \left( \frac{m_c(z)}{m_c(z_{\text{crit}})} \right)^H, \quad (4)$$

where  $B_\nu(T)$  is the Planck function at temperature  $T$ ,  $m_c(z)$  is the column mass at height  $z$  in the chromosphere, and  $H$  is a constant prescribed by Sollum (1999;  $H = 2$  for bound-bound transitions and  $H = 4$  for bound-free transitions). This equation is identical to Equation (3) of Leenaarts & Wedemeyer-Böhm (2006), but it differs from Equation (5.3) of Sollum (1999), where  $B_\nu(T_e(z_{\text{crit}}))$  is replaced by  $B_\nu(T_e(z))$ . The difference between the two is small, but the former is computationally simpler (J. Leenaarts 2017, private communication).

From Equation (3), we can solve for the brightness temperature  $T_b(z > z_{\text{crit}})$ ,

$$T_b(z > z_{\text{crit}}) = \frac{h\nu}{k_B} \left( \ln \left[ 1 + \frac{2h\nu^3}{J_\nu c^2} \right] \right)^{-1}, \quad (5)$$

where  $J_\nu$  is given by Equation (4).

We can now calculate the radiative coefficients at a given location and time using this prescription for the radiation field. Following Sollum (1999) as before, for radiative excitation with  $i < j$ ,

$$R_{ij} = \frac{8\pi^2 e^2 f_{ij}}{m_e c^3} \frac{\nu_0^2}{\exp\left(\frac{h\nu_0}{k_B T_b}\right) - 1}, \quad (6)$$

where  $e$  is the elementary charge,  $f_{ij}$  is the oscillator strength,  $m_e$  is the electron mass, and  $\nu_0$  is the rest frequency of the line. We take the atomic parameters like oscillator strengths, rest wavelengths, and statistical weights from Wiese & Fuhr (2009). The radiative de-excitation coefficient can be found

**Table 1**

The Brightness Temperatures at the Top of the Chromosphere for Each Transition  $i \rightarrow j$ , Derived by Sollum (1999), Table B.1 in That Work

$i \rightarrow j$	$T_b^{\text{top}}$ [K]
2 $\rightarrow$ 3	4500
2 $\rightarrow$ 4	4550
2 $\rightarrow$ 5	4500
3 $\rightarrow$ 4	4000
3 $\rightarrow$ 5	4300
4 $\rightarrow$ 5	3700
2 $\rightarrow$ 6	5493
3 $\rightarrow$ 6	4850
4 $\rightarrow$ 6	4750
5 $\rightarrow$ 6	4470

similarly,

$$R_{ji} = \frac{g_i}{g_j} \exp\left(\frac{h\nu_0}{k_B T_b}\right) R_{ij}, \quad (7)$$

where  $g_i$  is the statistical weight of level  $i$ .

The bound-free (radiative ionization) rate  $R_{ic}$  is calculated with a Kramers cross-section,

$$R_{ic} = \frac{8\pi\alpha_0\nu_0^3}{c^2} \sum_{q=1}^{\infty} E_1\left(\frac{qh\nu_0}{k_B T_b}\right), \quad (8)$$

where  $\nu_0$  is now the edge frequency,  $\alpha_0$  is the cross-section at  $\nu_0$ ,  $E_1$  is the first exponential integral, and  $q$  is just a summation index. We have evaluated this summation over the first 10,000 terms and found that the value of the sum has converged for all transitions in this study.

Finally, the free-bound (radiative recombination) rate  $R_{ci}$  is similar:

$$R_{ci} = \frac{8\pi\alpha_0\nu_0^3}{c^2} \left( \frac{n_i}{n_c} \right)_{\text{LTE}} \times \sum_{q=0}^{\infty} E_1\left( \left( \frac{qT_e}{T_b} + 1 \right) \frac{h\nu_0}{k_B T_e} \right). \quad (9)$$

We similarly sum over the first 10,000 terms here, again finding that all transitions in this work have converged. In this expression, the population ratio  $\frac{n_i}{n_c}$  is the LTE ratio, given by the Saha equation:

$$\left( \frac{n_i}{n_c} \right)_{\text{LTE}} = n_e \frac{g_i}{2g_c} \left( \frac{2\pi m_e k_B T_e}{h^2} \right)^{-3/2} \exp\left(\frac{h\nu_0}{k_B T_e}\right). \quad (10)$$

All of these coefficients are precalculated as lookup tables as functions of temperature(s) and density, as appropriate. In the simulations, we then interpolate the values using the local brightness temperature, electron temperature, and density.

## 2.2. Brightness Temperature

Since the thesis is not publicly available, in Table 1, we reproduce the list of the brightness temperatures at the top of the chromosphere  $T_b^{\text{top}}$  for each transition ( $i \rightarrow j$ ), derived for the VAL C model by Sollum (1999) from average quiet Sun observations (M. Carlsson 2018, private communication).

Since these values are based on the quiet Sun, however, we wish to scale them appropriately for flaring simulations. In

order to scale  $T_b^{\text{top}}$  with time, we first note that its value scales linearly with the intensity of the given line. Starting with Equation (3), we can solve to find

$$T_b = \frac{h\nu}{k_B \ln\left(1 + \frac{2h\nu^3}{J_\nu c^2}\right)} \approx \frac{c^2 J_\nu}{2k_B \nu^2}, \quad (11)$$

where we have expanded the logarithmic term to first order in the last step:  $\ln(1+x) \approx x$  for small values of  $x$ . The intensity of the line, then, can be used to scale the brightness temperature with time.

We have found empirically that the intensity of each line scales well with the footpoint density  $n_{\text{FP}}$  at the base of the transition region (where hydrogen transitions from neutral to ionized). We base this scaling on the more accurate treatment of radiative transfer from RADYN, using the publicly available simulations on the F-CHROMA website.<sup>3</sup>

For example, in Figure 1, we show the footpoint density variation with time (top), normalized brightness temperature variation with time for the six bound-bound transitions considered (center), and a scatter plot showing the relation between the two variables (bottom) for Model 045 in the database. In all six cases, there is a direct correlation between the footpoint density and the brightness temperature (with noticeable scatter). We disregard bound-free transitions because the brightness temperatures of these do not vary with time in the RADYN simulation. We fit a line in log-log space and rewrite the relation,

$$\log\left(\frac{T_b^{\text{top}}(t)}{T_b^{\text{top}}(t=0)}\right) = m \log n_{\text{FP}} + C, \quad (12)$$

$$T_b^{\text{top}}(t) = C(n_{\text{FP}})^m T_b^{\text{top}}(t=0), \quad (13)$$

where  $C$  is a constant, and  $m$  is the slope. This relation holds particularly well in simulations of intermediate-strength heating, where both the footpoint densities and brightness temperatures are sampled across a wide range of values. From Model 045, we find the following values of  $m$ , which we use in our approximation:

1. H $\alpha$ :  $m = 0.1188 \pm 0.0009$ .
2. H $\beta$ :  $m = 0.1116 \pm 0.0010$ .
3. H $\gamma$ :  $m = 0.1061 \pm 0.0011$ .
4. Paschen- $\alpha$ :  $m = 0.1460 \pm 0.0014$ .
5. Paschen- $\beta$ :  $m = 0.1402 \pm 0.0017$ .
6. Brackett- $\alpha$ :  $m = 0.1979 \pm 0.0026$ .

The values of  $C$  can be chosen such that the initial value of density  $n_0$  gives the initial brightness temperature:

$$T_b^{\text{top}}(t) = \left(\frac{n_{\text{FP}}}{n_0}\right)^m T_b^{\text{top}}(t=0). \quad (14)$$

We do not scale the temperatures to densities lower than the initial value.

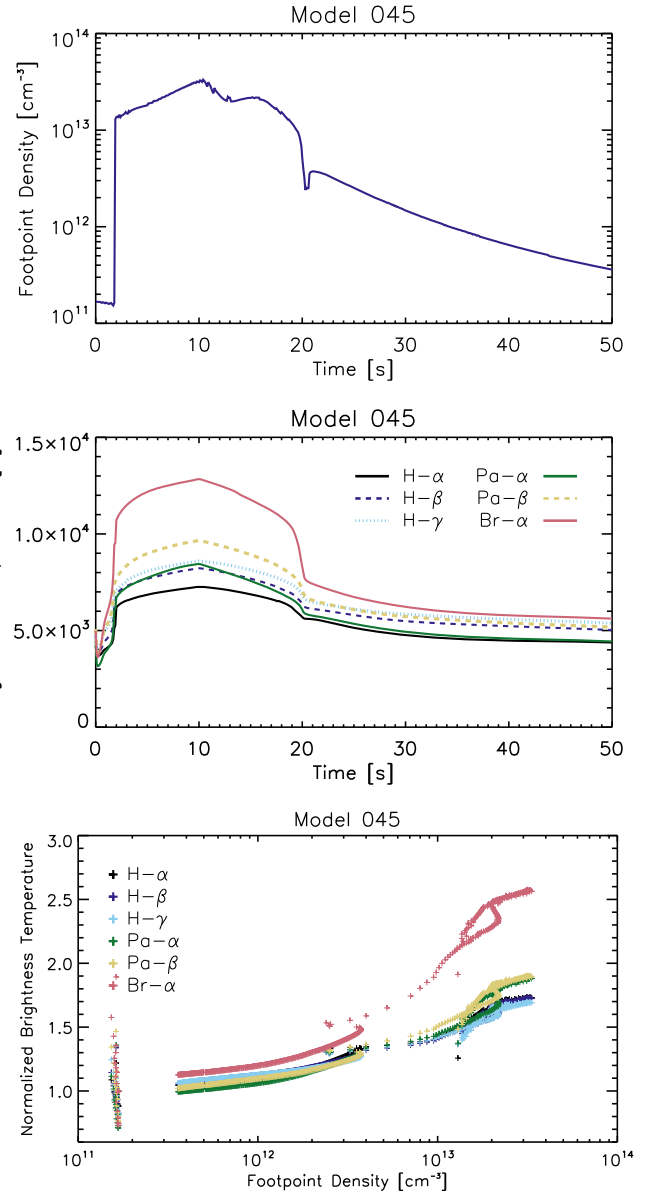


**Figure 1.** Scaling of brightness temperature  $T_b^{\text{top}}$  with footpoint density, using Model 045 from the F-CHROMA database. Top: footpoint density as a function of time. Center: brightness temperatures with time for the six bound-bound transitions under consideration. Bottom: scatter plot showing the relation between the two variables, with the brightness temperature normalized to its initial value. The brightness temperatures can be scaled directly in relation to the footpoint density.

In Figure 2, we compare the values of the brightness temperatures as a function of time in Models 078 and 012 in the database, as well as those calculated with the scaling relation in HYDRAD using the same simulation parameters. At most times, the footpoint densities in the simulations are comparable, so we find that the brightness temperatures are generally overestimated compared to the values in RADYN, particularly in the case with stronger heating (Model 012) by around 25% at the peak. As we show in the Appendix, though, the simulations are in good agreement with regard to densities, temperatures, and velocities, so the differences in brightness temperatures are acceptable. The slopes could perhaps be adjusted to improve the approximation, but that may not improve all cases uniformly, so we choose to use the above values.

<sup>3</sup> <https://star.pst.qub.ac.uk/wiki/doku.php/public/solarmodels/start>

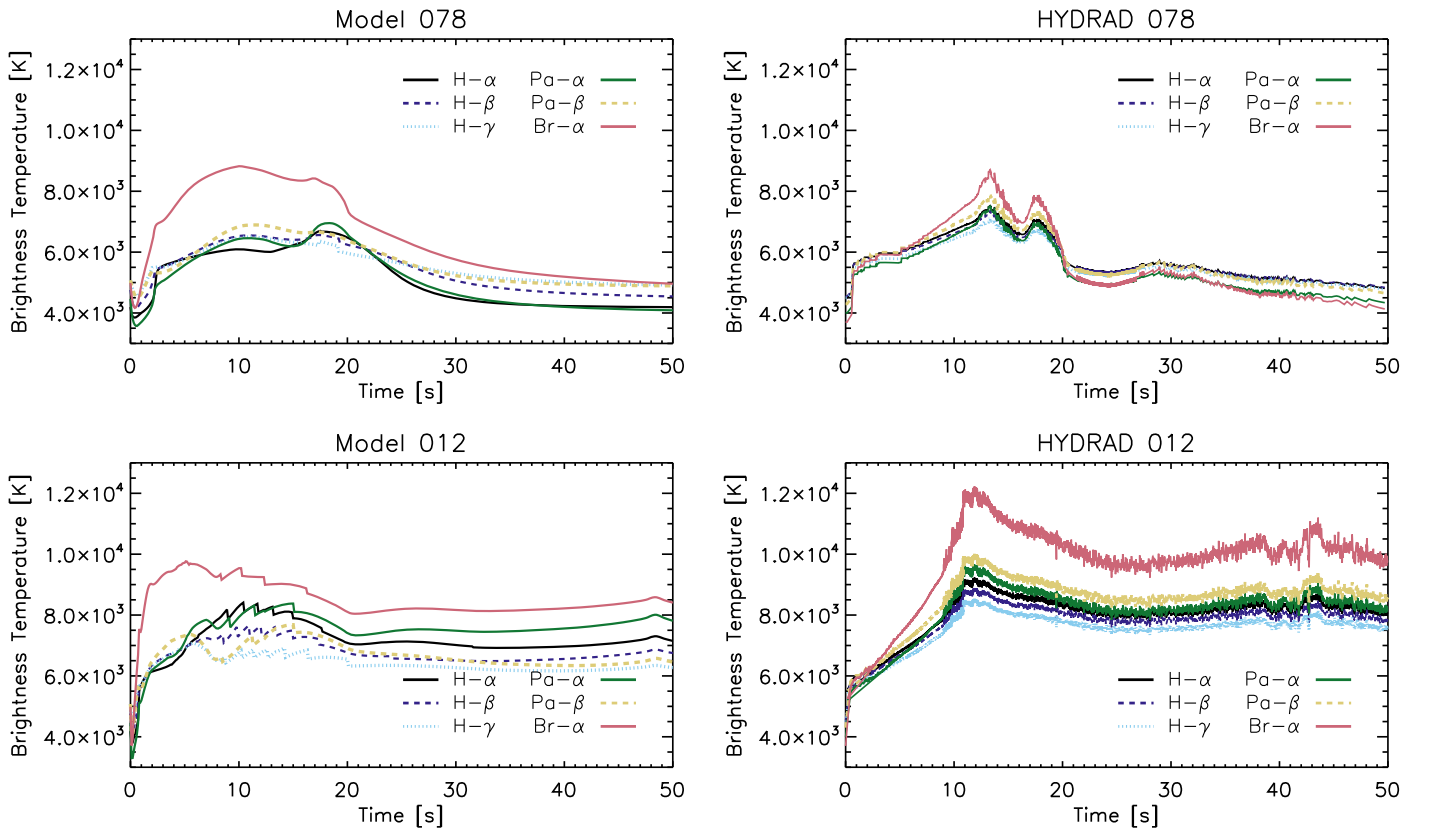


**Figure 2.** Brightness temperature with time for two simulations showing the values in RADYN (left) and HYDRAD (right). The approximation tends to overestimate the values, particularly in the case of stronger heating (Model 012). A full comparison of the hydrodynamics of these simulations is available in the [Appendix](#).

### 2.3. Nonthermal Collisional Excitation and Ionization

Collisions from nonthermal electrons with the ambient plasma can, in addition to heating the plasma, drive collisional excitation and ionization of the atoms. Previous studies have shown that this can have a nonnegligible effect on the level populations and line profiles of neutral hydrogen (Fang et al. 1993, 2003; Kašparová et al. 2009). Fang et al. (1993) found that this effect is most important for excitation and ionization from the ground state of hydrogen, and the effect of nonthermal collisions on excited states is negligible.

While the electron beam is active, therefore, we include nonthermal collisions in the rate equations. We follow Equation (22) in Allred et al. (2015),

$$C_{ij}^{\text{non-thermal}} = \zeta_{ij} \frac{\Lambda_n}{n_e \Lambda_i + n_H \Lambda_n} \frac{dE}{dt}, \quad (15)$$

where  $\zeta_{12} = 2.94 \times 10^{10}$ ,  $\zeta_{13} = 5.35 \times 10^9$ ,  $\zeta_{14} = 1.91 \times 10^9$ , and  $\zeta_{1c} = 1.73 \times 10^{10}$  (Fang et al. 1993);  $\Lambda_n$  and  $\Lambda_i$  are defined in Emslie (1978); and  $\frac{dE}{dt}$  is the energy deposition rate by the beam.

There are two noticeable effects when comparing simulations with and without this effect: the ionization fraction rises more quickly after the onset of heating, and the plasma ionizes at deeper depths. Since this affects the electron density at various heights in the chromosphere, chromospheric line profiles are also affected.

### 2.4. Level Populations

Once the rate coefficients have been calculated, we are ready to solve for the level populations. Equation (1) represents a set

of six equations, to which we add one constraint:

$$\sum_i n_i = 1. \quad (16)$$

This simply states that the sum of the fractional populations is 1.

We then have a  $7 \times 6$  matrix equation, which can be solved through singular-value decomposition (SVD). We use the SVD function taken from the *Numerical Recipes* text (Press et al. 2002) for this purpose. The matrix is not always well conditioned, so that SVD is the ideal choice for solving the matrix equation.<sup>4</sup>

There is one caveat: in general, we do not know the electron density prior to solving these equations, and the rate coefficients depend on the electron density. We therefore must make an initial guess as to the electron density and, through a gradient descent, iterate in small steps until the solution has converged.

The total electron density is given by the sum of the free electrons from hydrogen, helium, and metals. We approximate this using only the first 30 elements, as others are too scarce to contribute significantly:

$$n_e = n_H \times \left[ \frac{n_{H\text{II}}}{n_H} + \sum_{Z=2}^{Z=30} A_Z \left( \sum_{k=1}^{k=Z} k Y_k \right) \right], \quad (17)$$

where  $Z$  is the atomic number,  $A_Z$  is the fractional abundance of element number  $Z$ ,  $k$  is the ionization stage ranging from singly

<sup>4</sup> The pseudoinverse  $(A^T A)^{-1} A^T$  in the normal equation could also be used to solve the matrix equation in principle. Through simple tests, however, we have found SVD to be more robust for this application.

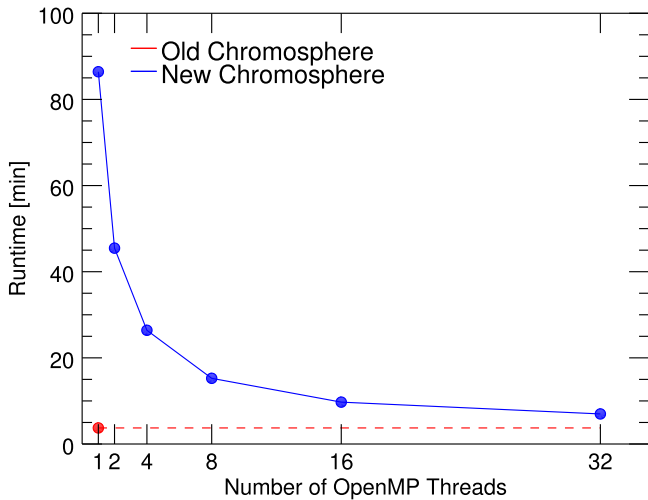


**Figure 3.** Comparison of run times for a simple simulation using the old version of the chromosphere (red) against the new chromosphere (blue) with various numbers of cores. The increase in speed scales as  $t \propto N^{-0.7}$  up to at least 32 cores and gets within a factor of 2 of the run time using the old chromosphere.

to fully ionized (e.g.,  $k = 2$  corresponds to doubly ionized), and  $Y_k$  is the fractional population of ionization stage  $k$  of element  $Z$ .

For trace elements, we solve for the ionization fractions  $Y_k$  either using an equilibrium calculation that is a function of temperature or by solving a continuity equation for nonequilibrium ionization states, as detailed in, e.g., Bradshaw & Mason (2003a, 2003b). The nonequilibrium solver can be used with all, some, or none of the elements, as determined by the user and appropriate for the study at hand.

The code makes an initial guess for the H II fraction, calculates the rate coefficients, solves Equations (1) and (16) for the level populations, and then recalculates the total electron density. The process iterates in small steps until the electron density has converged within a defined relative tolerance (default of  $10^{-6}$ ).

### 2.5. Radiative Losses

In previous versions of HYDRAD, the hydrogen and electron densities were essentially equal in the corona (with only a small correction for trace elements), so that the optically thin radiative losses  $E_R$  ( $\text{erg s}^{-1} \text{cm}^{-3}$ ) were approximated by setting  $n_e = n_H$ . We drop that approximation now and use the more accurate

$$E_R = -n_e n_H \Lambda(T_e), \quad (18)$$

where  $\Lambda(T_e)$  is the sum of the emissivity over all ions and all transitions for each ion (more precisely, all in the current version of CHIANTI; Del Zanna et al. 2015), and the minus sign indicates that the energy is lost from the system. The loss function  $\Lambda$  also depends on the ionization fractions and therefore also utilizes a nonequilibrium ionization calculation when desired.

In the chromosphere, we calculate radiative losses following the prescription of Carlsson & Leenaarts (2012), which calculates the loss of energy from hydrogen, calcium, and magnesium. We now use the ionization fraction of hydrogen determined by the above prescription in this calculation.

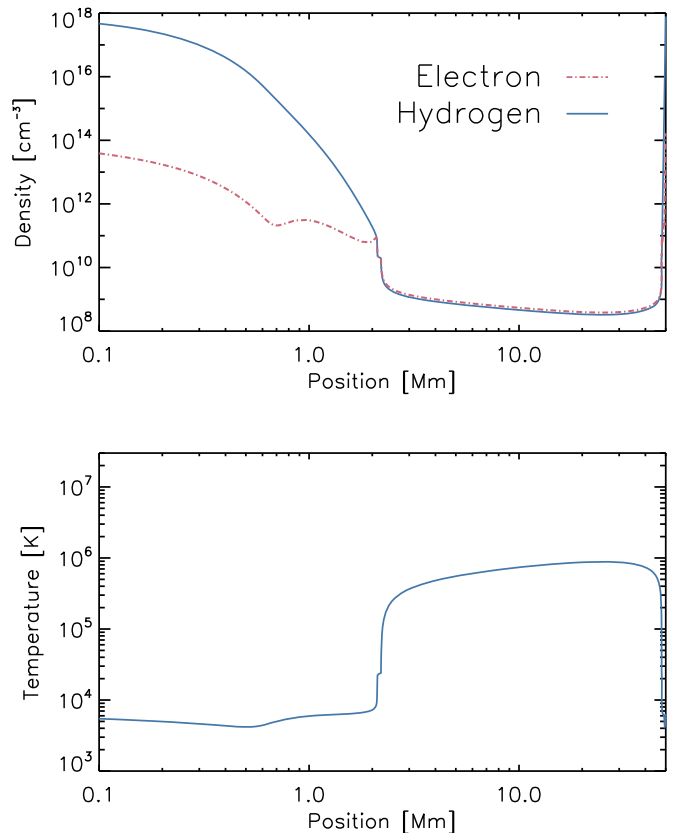


**Figure 4.** Hydrostatic density and temperature profiles for a loop of length  $2L = 50$  Mm. The temperatures are assumed to be initially equilibrated. Note that this figure (and others in this work) show the full loop, but the  $x$ -axis is shown on a logarithmic scale to emphasize the chromosphere. The electron density in the corona is slightly higher than the hydrogen density due to trace elements, while in the chromosphere, it is small due to the large fraction of neutral atoms.

### 2.6. Performance

The calculation of the NLTE level populations is a significant computational task. A few simple tests with various parameters have found that the code slows by a factor of 10–20 compared to previous versions. To offset these losses, HYDRAD has been recently parallelized with OpenMP. In Figure 3, we briefly show a timing test of the code. We have run an example simulation of electron beam heating (see the next section) with energy flux  $F_0 = 3 \times 10^9 \text{ erg s}^{-1} \text{cm}^{-2}$  for 10 s of heating. The simulations were only run for 100 s of simulation time. The timing of the simulation run with the older version of the chromosphere is shown in red, compared to the newer version of the chromosphere in blue. The improvements scale in time  $t \propto N^{-0.7}$ , where  $N$  is the number of cores requested, with improvements up to at least 32 cores. The resultant timing is within a factor of 2 of that using the original chromosphere.

## 3. Modeling

### 3.1. Initial Atmosphere

We now examine how these changes affect the dynamics of a coronal loop. We first examine the hydrostatic profile and then run a simulation with electron beam heating in order to look closely at the hydrodynamics.

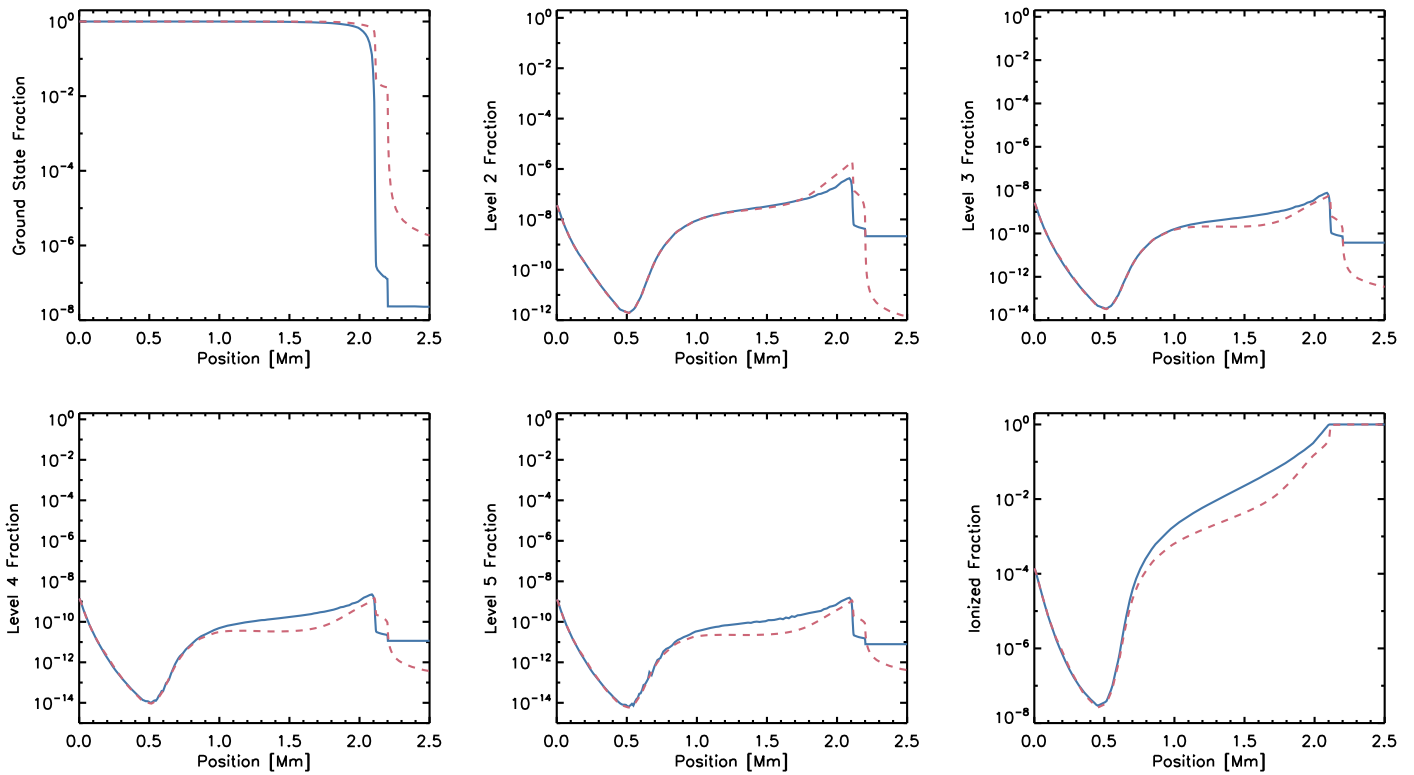


**Figure 5.** Hydrostatic hydrogen level populations as calculated by the HYDRAD solver (blue solid lines) following the description in Section 2 and by RH1.5D (red dashed lines). The two methods show good agreement deep in the chromosphere, while the ionized fraction is overestimated in the upper chromosphere.

To begin, we calculate the initial conditions for a given coronal loop. Using the VAL C chromospheric temperature profile (Vernazza et al. 1981), we generate a chromospheric density profile by solving the hydrostatic equations with the above prescription to solve for the electron density along the full loop from footpoint to footpoint, which is assumed to be symmetric in this work in both geometry and heating. In Figure 4, we show the temperature and density profiles of a loop with length  $2L = 50$  Mm. The electron and hydrogen temperatures are assumed to be initially equilibrated. In the corona, the electron density is higher than the hydrogen density due to the electron contribution from trace elements. In the chromosphere, where the ionization fractions are much lower, the electron density is orders of magnitude lower than the hydrogen density.

The level populations for the six-level hydrogen atom in the chromosphere of one of the footpoints are shown in Figure 5. We show the levels as calculated by the HYDRAD solver (using the Sollum 1999 method), shown as solid lines, as well as the level populations calculated by the RH1.5D code (Pereira & Uitenbroek 2015), shown as dashed lines. Deep in the chromosphere and nearing the photosphere, the two methods agree almost exactly because the plasma is in collisionally dominated LTE. In the chromosphere, however, the radiation field is more significant. HYDRAD predicts a higher ionized fraction near the top of the chromosphere and thus a lower neutral fraction, which in turn means that the electron density is likely overestimated in the upper chromosphere. In the corona, the plasma is essentially fully ionized in both cases, though the methods disagree.

### 3.2. Hydrodynamics

To understand how the parameters vary over time, we now run a dynamic simulation. We impose heating due to an electron beam (Reep et al. 2013, 2016a), assuming a constant energy flux  $F_0 = 3 \times 10^{10} \text{ erg s}^{-1} \text{ cm}^{-2}$ , sharp low-energy cutoff  $E_c = 15$  keV, and spectral index  $\delta = 5$ , for a total of 10 s. Figure 6 shows the hydrodynamics of that simulation: from top to bottom and left to right, the electron density, electron temperature, hydrogen density, hydrogen temperature, electron heating rate (including the background heating term), and bulk flow velocity of the plasma. All are shown at a 1 s cadence from purple to red, and the black dotted line marks the initial transition region. The strong heating event quickly raises the electron temperature at the top of the chromosphere and in the corona (to about 20 MK), which causes the plasma to strongly ionize, liberating electrons from the mostly neutral plasma and increasing the electron density. The increased pressure in the chromosphere quickly drives a strong and explosive evaporation event, carrying significant amounts of plasma into the corona, as well as driving a slower condensation deeper into the chromosphere. The hydrogen temperature slowly equilibrates through collisions between the hydrogen and electrons.

For that same simulation, in Figure 7, we show the evolution of each of the six level populations with time during the heating period at a 1 s cadence from purple to red. The heating to the beam quickly raises the temperature of the chromosphere, which causes a sharp rise in the ionized fraction there. Increased collisional excitation due to the increased electron density also causes sharp spikes in the higher-level states to form at the same location. As chromospheric evaporation

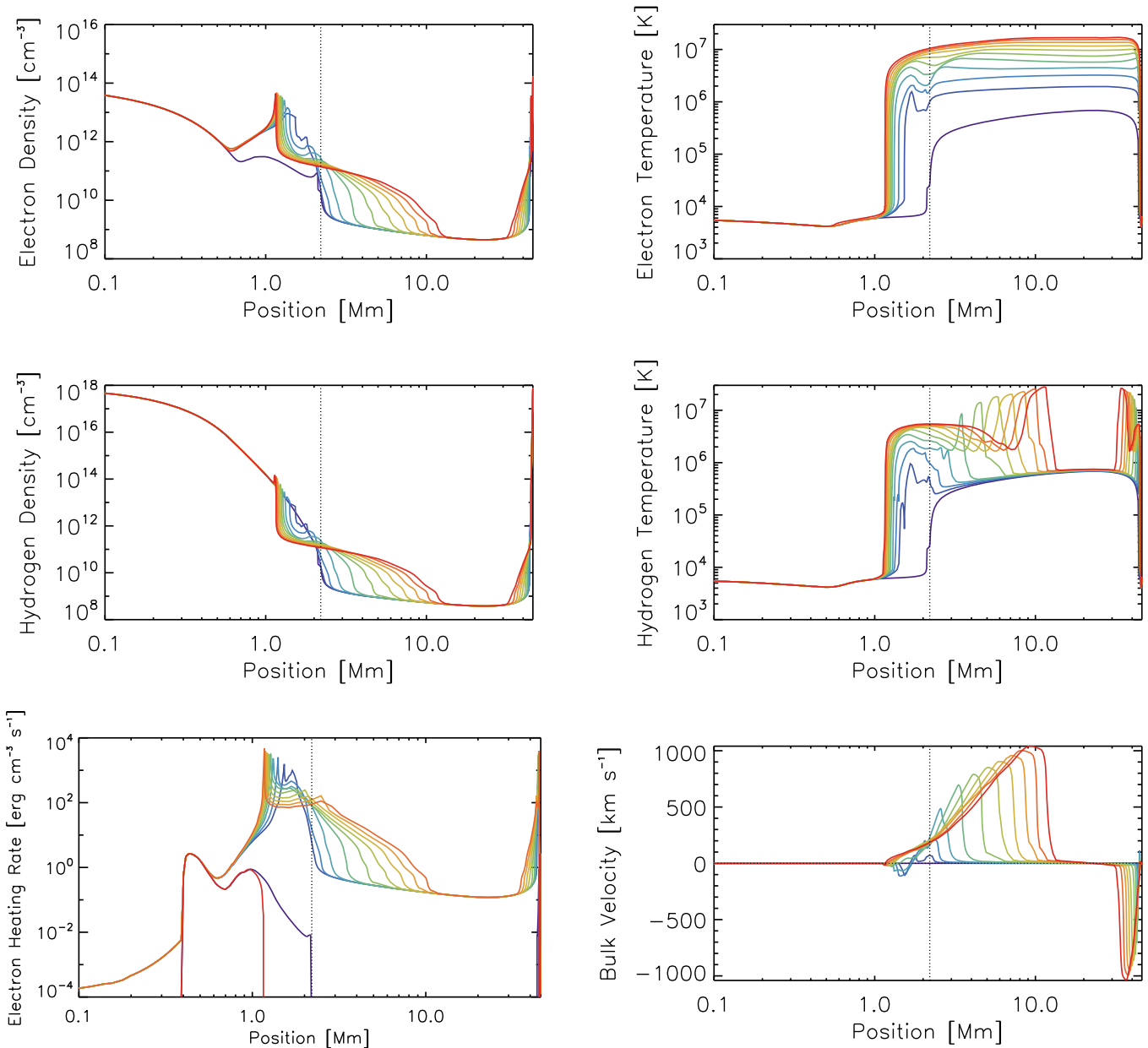


**Figure 6.** Hydrodynamics of a loop heated for 10 s by an electron beam with  $F_0 = 3 \times 10^{10} \text{ erg s}^{-1} \text{ cm}^{-2}$ , sharp low-energy cutoff  $E_c = 15 \text{ keV}$ , and spectral index  $\delta = 5$ . The electron and hydrogen temperatures and densities are shown, along with the rate of energy deposition by the beam (plus the background heating term) and the bulk flow velocity. All plots show a 1 s cadence from purple to red. The dotted black line marks the initial transition region, and velocities traveling to the right are defined as positive. The heating quickly causes a sharp ionization in the chromosphere, and the increased pressure drives a strong, explosive evaporation event. An animation of the six plots is available in the electronic version of the manuscript, showing the first 25 s of the simulation.

(An animation of this figure is available.)

begins to carry material into the corona, neutral hydrogen from all levels is advected into the corona, though the hydrogen remains nearly fully ionized.

A natural question is to ask how the approximation compares to a more detailed calculation of the levels. We have therefore calculated the level populations using a full radiative transfer solution via RH1.5D. In Figure 8, we show a comparison of the level populations at times 0, 2, 4, 6, 8, and 10 s into the simulation as calculated both using the method in Section 2 and by RH1.5D itself (which will be used to forward model the emissions). We show the first 2.5 Mm of the loop (the chromosphere to the bottom of the corona) with all six levels. At time 0 s, the two methods agree in the deep chromosphere

( $\lesssim 1.0 \text{ Mm}$ ), while they disagree in the upper chromosphere by a factor of up to 5 or so (most notably in the ionized fraction). At later times, the methods diverge in the upper chromosphere, primarily because of the effect of nonthermal collisional ionization and excitation, which drastically alters the populations from their static solutions (which RH1.5D assumes). When the heating ceases, at time 10 s, the nonthermal effect also ceases, and the two are found to be in reasonable agreement at all heights. One other important difference to note is that RH1.5D assumes a static atmosphere, meaning that time and advective gradients are not included in the calculations, though the electron densities in the simulation reflect those effects. Therefore, there are important differences here that



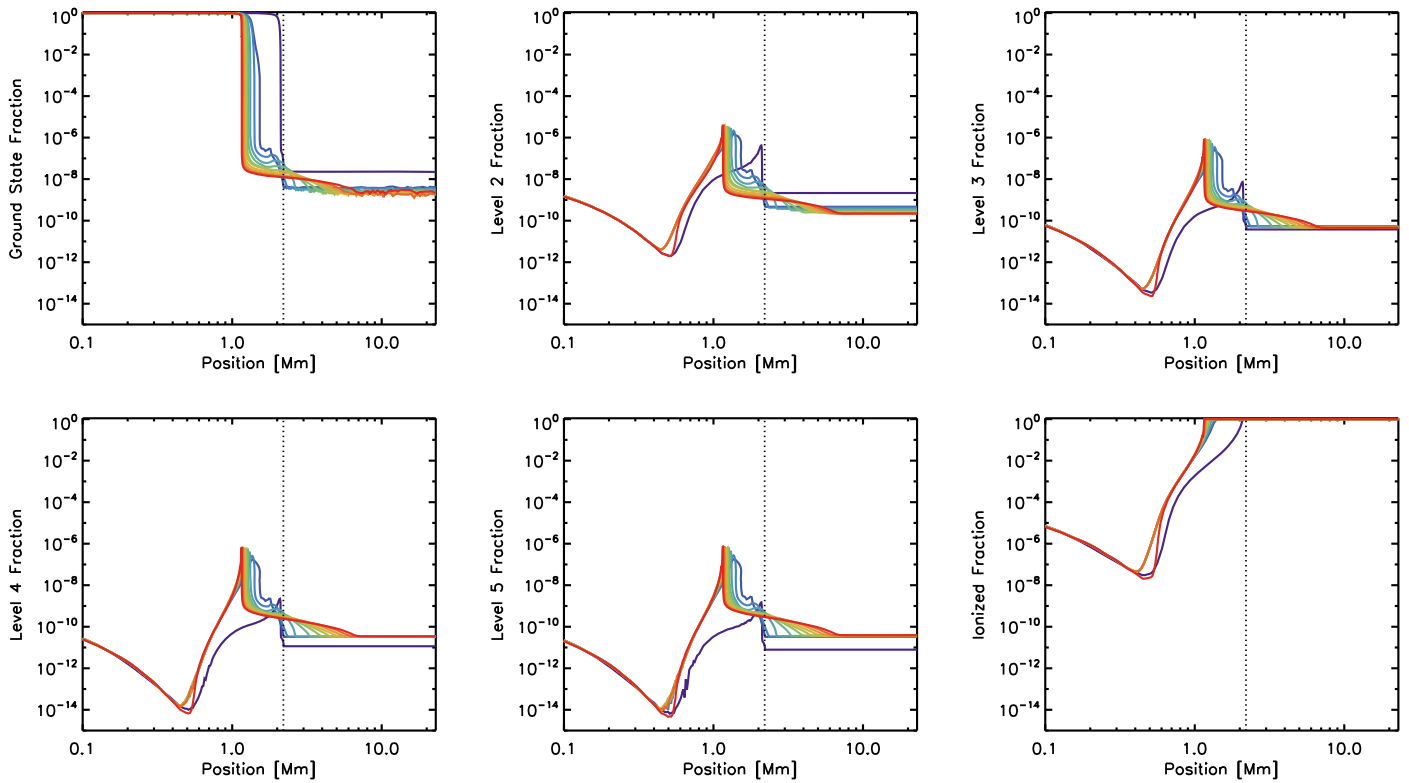


**Figure 7.** Evolution of the fractional level populations of hydrogen for the duration of heating during an electron beam-heating simulation, shown at 1 s cadence from purple to red. The dotted black line marks the initial transition region. The chromosphere quickly becomes fully ionized, reducing the fraction of neutral hydrogen in the ground state significantly while also exciting the upper levels. Advection carries neutral hydrogen from the first five levels into the corona, though it remains strongly ionized. An animation of this figure is available in the electronic version of the manuscript, showing the first 25 s of the simulation.

(An animation of this figure is available.)

should be kept in mind while examining the results of forward modeling.

#### 4. Forward Modeling

The true test of any model is its ability to reproduce observations, so we therefore turn to forward modeling the spectral data seen with *IRIS*. We consider the 2014 November 19 UT 14:14 flare, which was the focus of Warren et al. (2016), and attempt to model emission from O I, C II, and Mg II. In Reep et al. (2016b), it was found that while Si IV emission could be accurately reproduced with optically thin calculations, the observed strong stationary component of C II was not found in the model. It was found that Mg II had bursts in intensity and was weakly redshifted during the heating period, though the modeling did not attempt to reproduce this line.

Warren et al. (2016) observed the O I 1355.598 Å line, but it was not shown explicitly in the paper, so we present it here before synthesizing the line with a forward model. Figure 9 shows the intensity, Doppler shift, and Gaussian line width, calculated with the moments of the line (as explained in Warren et al. 2016). On the left, these quantities are shown as a function of time along the slit; on the right, they are shown at a single pixel marked by a dashed pink line. During the event, the line brightens but remains essentially stationary relative to the background. There is also no noticeable broadening associated with the brightening.

Attempts to reproduce this line using optically thin assumptions (i.e., the method in Reep et al. 2016b) result in a line that is consistently redshifted during the heating period,

like Si IV and C II. One possible explanation of this is that we have disregarded NLTE and/or opacity effects by using optically thin assumptions. Therefore, in order to attempt to explain this line, we follow the basic methodology of Reep et al. (2016b): we run many simulations to create a multi-threaded model, from which we calculate light curves and line profiles. Instead of synthesizing the line with optically thin assumptions, however, we use RH1.5D (Pereira & Uitenbroek 2015), which solves a full radiative transfer calculation at a given time snapshot, including important NLTE and opacity effects. Though O I is our primary focus, we also synthesize C II and Mg II emission to contrast with observations.

We have therefore run hydrodynamic simulations with HYDRAD of loops subjected to heating by electron beams, following the parameter space of Reep et al. (2016b). We use energy fluxes ranging from  $10^8$  to  $10^{11}$  erg s<sup>-1</sup> cm<sup>-2</sup> and the *RHESSI*-derived low-energy cutoff  $E_c = 11$  keV and spectral index  $\delta = 6$  (see Reep et al. 2016b for the *RHESSI* data). We arbitrarily assume a heating duration lasting 10 s following that paper in order to facilitate the comparisons, but in the more recent paper Reep et al. (2018), it was found that 10 s is insufficient to reproduce the Fe XXI Doppler shift observations seen in much larger flares, which seem to require durations averaging between 50 and 100 s.

On all of these simulations, we have run RH1.5D to calculate each line profile for O I 1355.598 Å, C II 1334.535 Å, and Mg II 2796.354 Å. Mg II is calculated with partial redistribution (PRD), which is particularly important for this transition (Leenaarts et al. 2013), using the “PRD\_ANGLE\_APPROX”

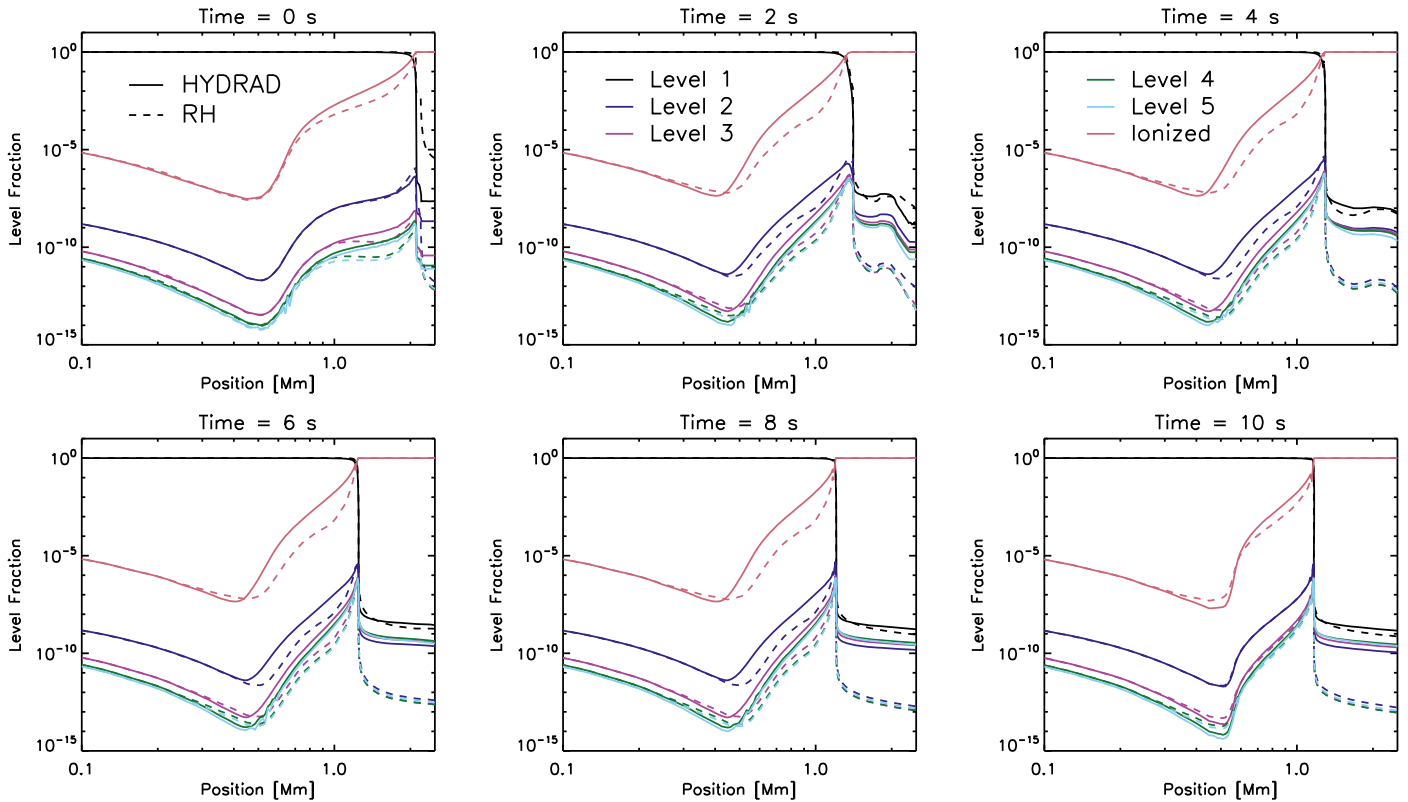


**Figure 8.** Comparison of the hydrogen level populations as computed by the method outlined in Section 2 (solid lines) and by RH1.5D (dashed lines). The two methods disagree in the upper chromosphere during the heating period, primarily due to the effect of nonthermal ionization and excitation, which RH1.5D does not account for. The two methods also disagree in the corona, though the change in the resultant electron density is negligible. Please note that RH1.5D uses the output from HYDRAD as input and assumes a static atmosphere, which is not a self-consistent comparison. In the Appendix, we therefore include a detailed comparison to another numerical model.

scheme in RH1.5D (Leenaarts et al. 2012). We treat the other lines with complete redistribution (CRD). We ran RH1.5D with five atoms: H, O, C, and Mg as active and He as passive (i.e., only used as a source of background opacity). We truncated the loop at the size of an *IRIS* pixel, approximately 240 km on the Sun ( $\approx 2.6$  Mm in field-aligned coordinates with a 46 Mm loop).

Following Warren et al. (2016), we subtract the continuum near each line and then calculate the moments of each line. Because RH1.5D produces intensities in absolute units, we convert to DN by convolving the output with the *IRIS* response, obtained from the SolarSoftWare IDL routine “iris\_get\_response.” In this way, the intensities are directly comparable to the observed values. All wavelengths are listed in vacuum wavelengths.<sup>5</sup> For these lines, we assume a  $3 \text{ km s}^{-1}$  micro-turbulence value.

As an example, consider the simulation in the previous section, with energy flux  $F_0 = 3 \times 10^{10} \text{ erg s}^{-1} \text{ cm}^{-2}$ , whose hydrodynamics were shown in Figure 6. We calculate the line profiles and light curves for each of the three lines, shown in Figure 10. The line profiles (O I, C II, Mg II, and H $\alpha$ ) are shown at a 1 s cadence for the first 20 s of the simulation. Each brightens significantly during the heating period and begins to dim as cooling begins. Initially, all four show a redshift due to a strong red-wing component (up to  $\approx 100 \text{ km s}^{-1}$ ), which most

strongly affects the C II line. There are two obvious discrepancies with the observational data, however: the C II redshifts are short-lived ( $\approx 30$  s), and the O I line is much brighter (and wider) than observed. RH1.5D assumes statistical equilibrium and disregards the level populations from HYDRAD, which means that the O I populations could be affected, since they are sensitive to charge exchange (Lin & Carlsson 2015). That the C II redshifts are so short-lived reiterates a major fault of single-loop models, which predict only short-lived chromospheric condensations. H $\alpha$  is shown in absolute units, since it is not observed by *IRIS*, but its development can be compared to, e.g., Kuridze et al. (2015). The relative brightenings are large compared to that work, the line width is too narrow (see Kowalski et al. 2017b for the likely explanation), and there is no apparent central reversal (compare Rubio da Costa et al. 2015).

In order to improve the results, we appeal to the multi-threaded model. We have written an IDL routine that creates a multithreaded line profile as a function of time that can be used to then calculate the light curves and Doppler shifts. As in Reep et al. (2016b, 2018), we select the total number of threads  $N$  and the average waiting time between new threads  $r$  (using a Poisson distribution). We select energy fluxes from a power law, with the index of the energy distribution  $\alpha$  and the minimum energy flux on that energy distribution  $F_{\text{min}}$ . In all cases, we choose  $N \times r = 600$  s, which is the approximate duration of the hard X-ray burst. The low-energy cutoff and spectral index of the injected electron distribution were derived from *RHESSI* data (shown in Reep et al. 2016b). Finally,

<sup>5</sup> O I has a rest wavelength of  $1355.598 \text{ \AA}$  according to both the CHIANTI and NIST databases, but the model atom in RH1.5D produces a rest wavelength of  $1355.63 \text{ \AA}$ , which amounts to  $\approx 7 \text{ km s}^{-1}$  difference. This has been corrected for in this work.

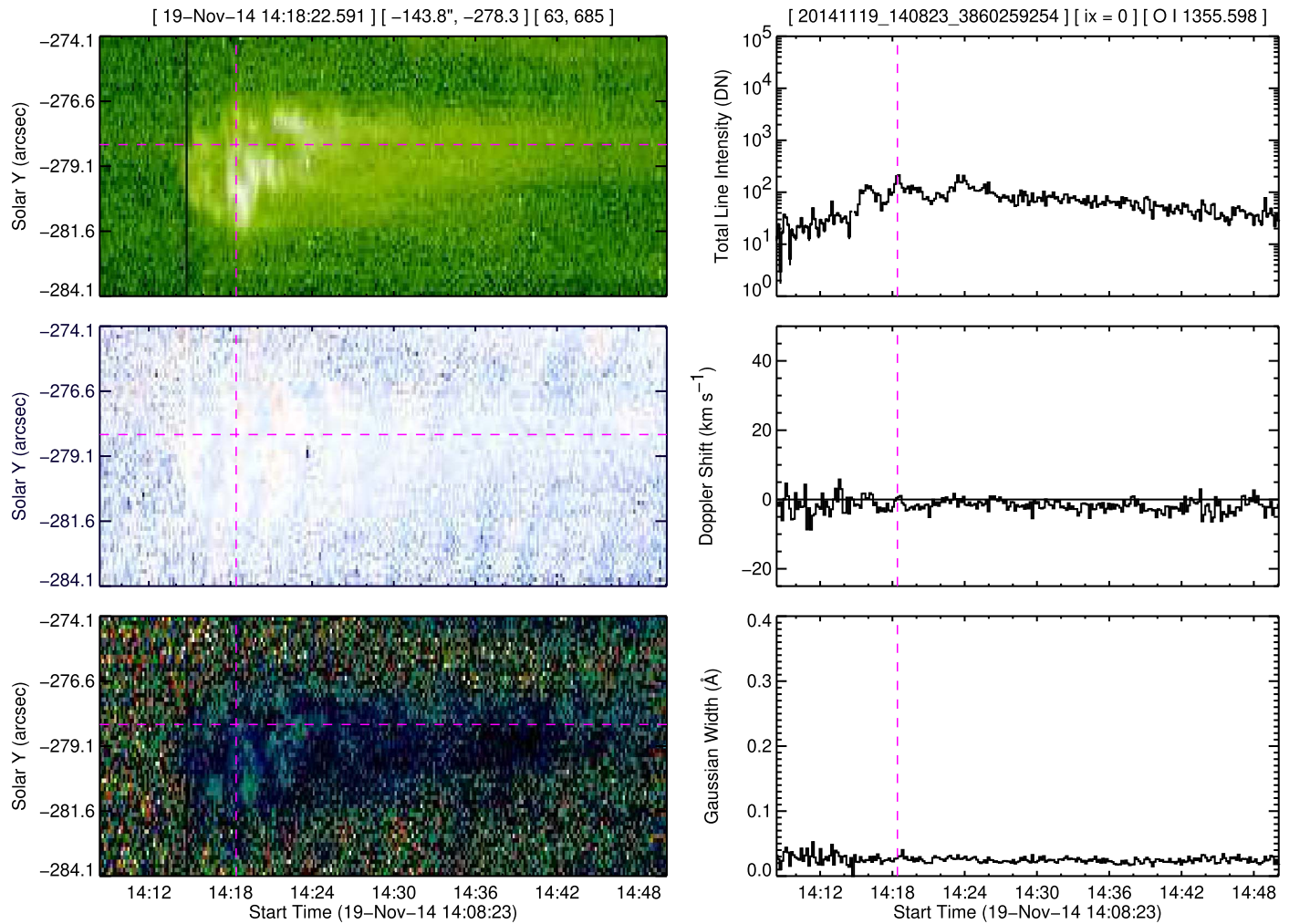


**Figure 9.** Intensities, Doppler shifts, and Gaussian line widths determined from moments of the O I 1355.598 Å line. The line remains close to stationary at all times relative to the background, with small variations up to about  $5 \text{ km s}^{-1}$ . The intensity rises by about a factor of 10 up 100–200 DN, while the line width remains essentially constant. The left panels show these parameters along the slit as a function of time, while the right panels show the values at a given pixel (marked by the dashed pink line). Note that the range of line widths displayed here is much narrower than those displayed in Warren et al. (2016).

because we assume that all threads are rooted within 1 pixel, we divide the total intensity by  $N$ , which equivalently says that each has a cross-sectional area equal to the pixel area divided by  $N$ . We wish to stress that because there are multiple random variables, the results can change even using the same parameters, but the trends remain essentially unchanged.

We begin with parameters that were deemed a good fit in Reep et al. (2016b):  $N = 120$  threads,  $r = 5 \text{ s}$  per thread, and  $F_{\min} = 3 \times 10^9 \text{ erg s}^{-1} \text{ cm}^{-2}$ . Figure 11 shows three cases with spectral indices  $\alpha = -1, -1.5, \text{ and } -2$ . In all three cases, O I is stationary, with only small bursts of redshifts ( $2\text{--}3 \text{ km s}^{-1}$ ), but its intensity is too bright by about a factor of 10. Here C II shows strong redshifts that begin with the onset of heating, up to  $30 \text{ km s}^{-1}$ , gradually decaying in magnitude, until the redshifts finally cease after the heating period. Its intensity grows smoothly, reaching peaks of between 10 and 100 kDN, slightly lower than the observed peak of 100 kDN (though the average value was closer to 10 kDN). Similarly, Mg II forms a strong initial redshift ( $\approx 10 \text{ km s}^{-1}$ ) that decays gradually over the heating period, averaging values less than  $5 \text{ km s}^{-1}$ . Its intensity rises slightly, to levels of 10–20 kDN, without much variation. The peak intensity in all cases is smaller than the observed value, which reached as high as

100 kDN, with a background level of about 10 kDN. In general, the behavior shows good agreement with the observed trends, though the intensities vary and do not agree completely with the observations. In particular, the ratio of O I to C II is approximately constant, and the parameters only seem to reproduce one or the other at a given time. This may be due to the assumptions of the beam heating (e.g., fixed cutoff energy on all threads, short duration heating, etc.); the assumed values of  $N$ ,  $\alpha$ , or  $F_{\min}$ ; or, perhaps, the assumptions about the initial atmosphere. The beam-heating parameters (low-energy cutoff and spectral index), however, were taken from fits to the *RHESSI* data for this event, so it is unlikely that they are the issue.

Figure 12 shows a bit more of the parameter space, with  $N = 60, 300, \text{ and } 600$  (left to right) and  $F_{\min} = 10^8 \text{ and } 3 \times 10^9 \text{ erg s}^{-1} \text{ cm}^{-2}$  (top and bottom rows). As in Reep et al. (2016b), we find that the persistent redshifts seen in C II are consistent with a large number of threads with high median energy flux. Here O I generally shows little or no shift ( $\lesssim 5 \text{ km s}^{-1}$ ), while Mg II has shifts up to  $10 \text{ km s}^{-1}$  that gradually decay with time, which is consistent with observations. As in Figure 11, we find that the ratio of intensities between C II and O I is approximately constant, such that either

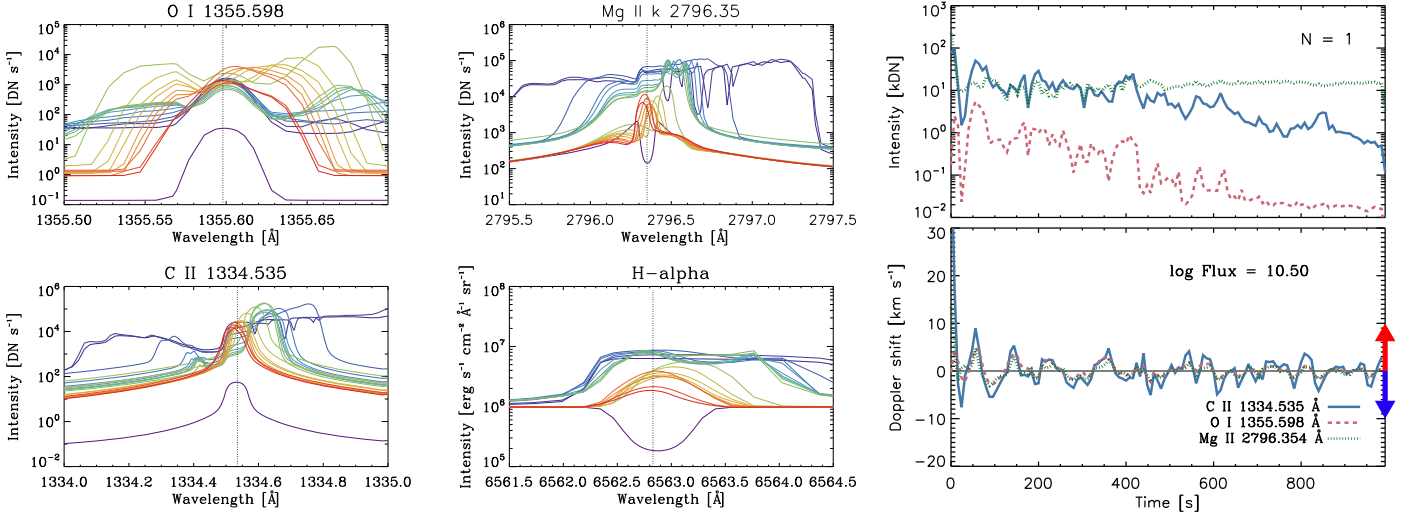


**Figure 10.** Light curves and line profiles for the single thread simulation shown in Figure 6. At left, we show the line profiles (O I, C II, Mg II, and H $\alpha$ ) for the first 20 s of the simulation, shown as different colors ranging from purple to red at a 1 s cadence. At right, we show the light curves and Doppler shifts calculated from the moments of each line. These assume a filling factor of 1. This simulation is inconsistent with the observations because there is no persistent redshift in C II, there is no gradual decay of redshift in Mg II, and the intensity of O I is too large.

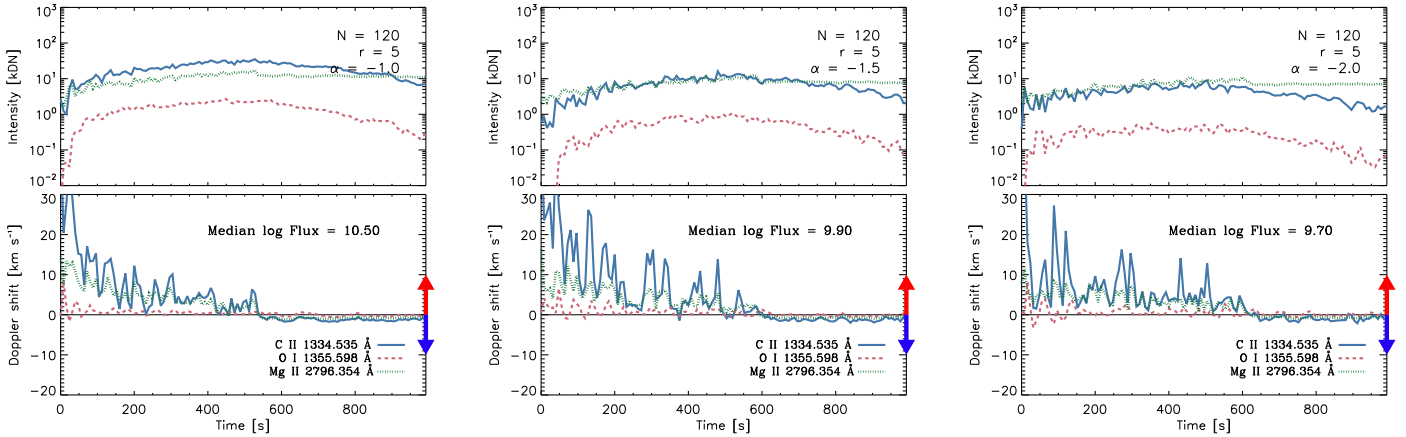


**Figure 11.** Multithreaded light curves and Doppler shifts for the three spectral lines under consideration, synthesized by RH1.5D, using  $N = 120$  threads,  $r = 5$  s per thread on average, and  $F_{\min} = 3 \times 10^9 \text{ erg s}^{-1} \text{ cm}^{-2}$ . From left to right, each uses a spectral index of the power-law distribution of energies  $\alpha = -1, -1.5,$  and  $-2$ . Redshifts are defined as positive. The Doppler shifts are in general agreement with the observations: O I is essentially stationary in all cases, while C II is strongly redshifted during the heating period, and Mg II is weakly redshifted. The intensities of C II and Mg II are roughly consistent with the observed values, but the intensity of O I is larger than observed.

C II is too dim or O I is too bright, again suggesting that the initially assumed atmosphere differs from actual solar conditions.

While it seems that the basic model can reproduce many of the observed features of the event, it seems likely that the initial chromospheric density and temperature profile are not consistent with actual solar conditions, suggesting that perhaps a tuning of the atmosphere would better reproduce the observables. For example, a recent study by Ishikawa et al. (2018) found that Hanle effect diagnostics depend strongly on the choice of atmospheric model. With the high cadence and high spatial resolution observations of lines such as Ly $\alpha$  (e.g., Ishikawa et al. 2017), it may be possible to directly tune the initial atmosphere for events under examination in the future. We therefore briefly examine how altering the chromospheric model affects the synthesized line profiles, as compared to observations.

In Figure 13, we show nine transition regions and chromospheric lines that can be used as diagnostics of the atmospheric density and temperature profile (left to right, top to bottom): Ly $\alpha$ , Ly $\beta$ , He I 584 Å, He I 304 Å, He II 256 Å, O I 1355.6 Å, C II 1334.4 Å, Mg II k 2796.4 Å, and Mg II h 2803.5 Å. In this figure, the Lyman lines and Mg II were calculated in PRD, while the others were done with CRD. The solid pink curves show the spectral lines as synthesized by RH1.5D using the VAL C temperature profile, with the default density profile derived from HYDRAD and no microturbulence, while the solid blue curves show a case where we have decreased the footpoint density by a factor of 1.5 and solved the hydrostatic equations again to produce a new density profile that more closely matches the peak intensity of Ly $\alpha$ , with an assumed microturbulence of 6 km s $^{-1}$ . The dashed black curves show example quiet Sun profiles measured by SUMER, a rocket flight reported by Doschek et al. (1974), EIS, or IRIS, as

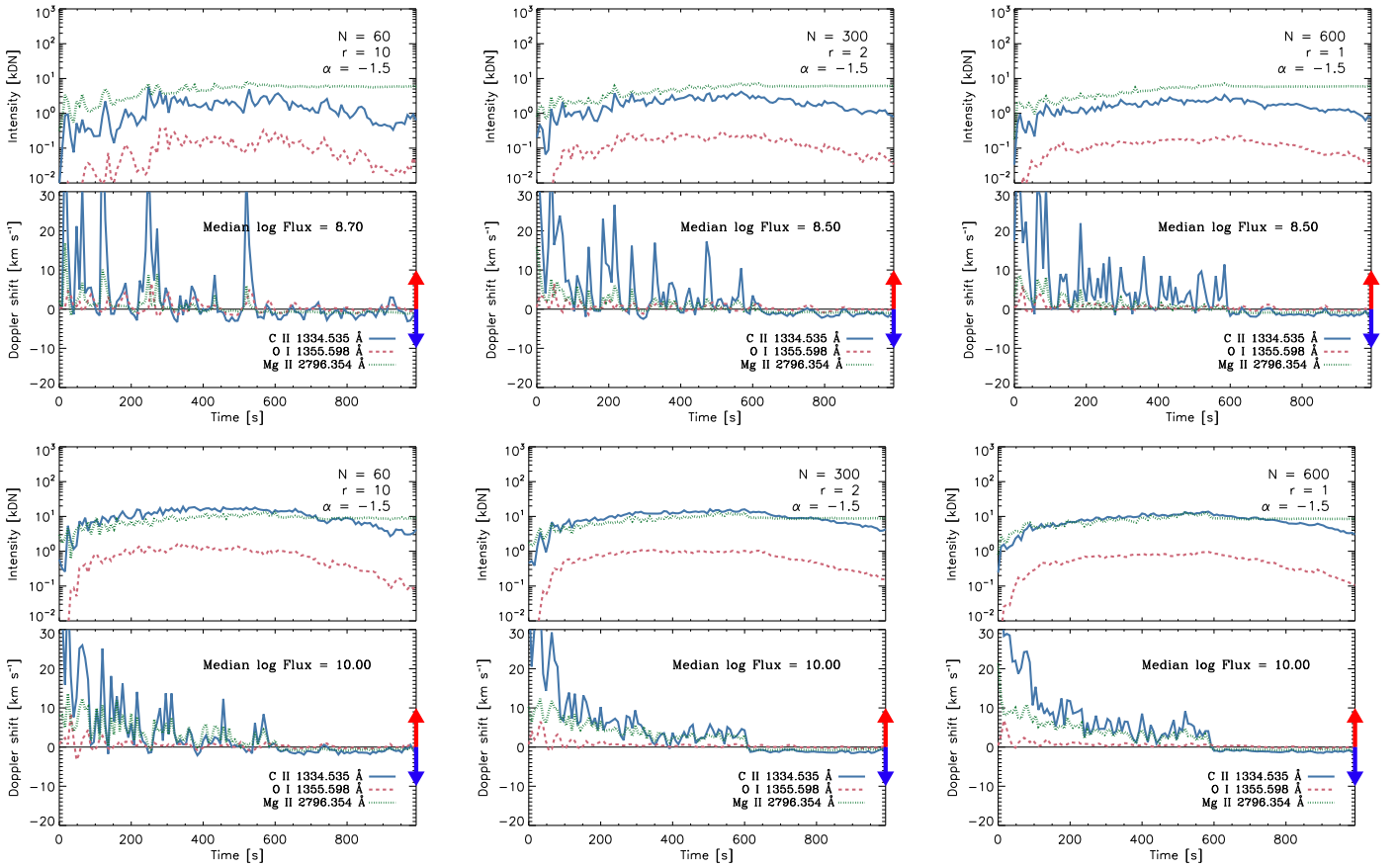


**Figure 12.** Similar to Figure 11. The top row shows  $F_{\min} = 10^8$  and the bottom  $3 \times 10^9$  erg s $^{-1}$  cm $^{-2}$ , while the columns show  $N = 60, 300,$  and  $600$  threads (left to right). As with the previous figure, the results are mostly consistent with observations, in that the persistent redshifts in C II are consistent with a large number of threads with high median energy flux, while O I is close to stationary, but the problem remains that O I is too bright.

indicated in the plot. We have convolved each synthesized case with the instrumental line width of each respective instrument.

It is clear that *none* of the model atmospheres reproduces any of the observed profiles in all of the lines simultaneously. In the solid blue case, where we have reduced the footpoint density and solved the hydrostatic equations again to improve agreement with the observed intensity in Ly $\alpha$ , we generally find that the agreement of lines that form at other heights can either improve or worsen. To emphasize this, we show the wavelength-integrated intensities (over the range in the plots) in Table 2, which demonstrates that none are in particularly good agreement. We have also included the integrated intensities synthesized with RH1.5D from the FAL C (Fontenla et al. 1993) model atmosphere as a basis for comparison. This suggests that the temperature profile is inaccurate, or perhaps that a hydrostatic profile may never accurately reproduce the chromosphere lines. It is likely that we also need a turbulence value as a function of height in the chromosphere to better match the observed broadening.

In order to better constrain future simulations, we suggest that the preflare atmosphere (time 0 in the simulations) should be tuned to preflare observations. Reep et al. (2016a) reached similar conclusions concerning the modeling of X-ray source heights in a flare. While the chromosphere is inherently dynamic, having a good initial agreement between the real and model atmosphere improves the confidence that our initial assumptions about the atmospheric profile do not adversely affect the hydrodynamic and forward-modeling results.

Spectral polarimetric inversion models have been shown to produce chromospheric profiles (Socas-Navarro et al. 1998, 2000), determining temperature, turbulence, velocity, and magnetic field strength as functions of depth. In a forthcoming paper, we plan to develop a similar method to therefore tune the preflare atmosphere used in simulations to give good agreement with preflare observations. We expect that future instruments such as DKIST or Solar-C may prove fruitful in this regard.

## 5. Conclusions

In this work, we have examined the importance of NLTE effects on the formation of light curves and Doppler shifts. In general, a model of the dynamic chromosphere requires a detailed treatment to determine ionization fractions and level populations. Solving the radiative transfer equation in general is one of the most computationally demanding tasks in astrophysics, primarily due to its non-local nature.

In solar flares, there are many indications that there is substructuring at spatial resolutions below those of current instrumentation. This led to the rise of multithreaded models, where many unresolved loops are assumed to be rooted within a single pixel. Originally, this type of modeling was invoked by Hori et al. (1997, 1998) to explain the large stationary component of Ca XIX seen in flare observations with *Yohkoh*/BCS, where strong blueshifts were expected from single-loop modeling of evaporation flows. Later papers addressed other problems with long-duration cooling of soft

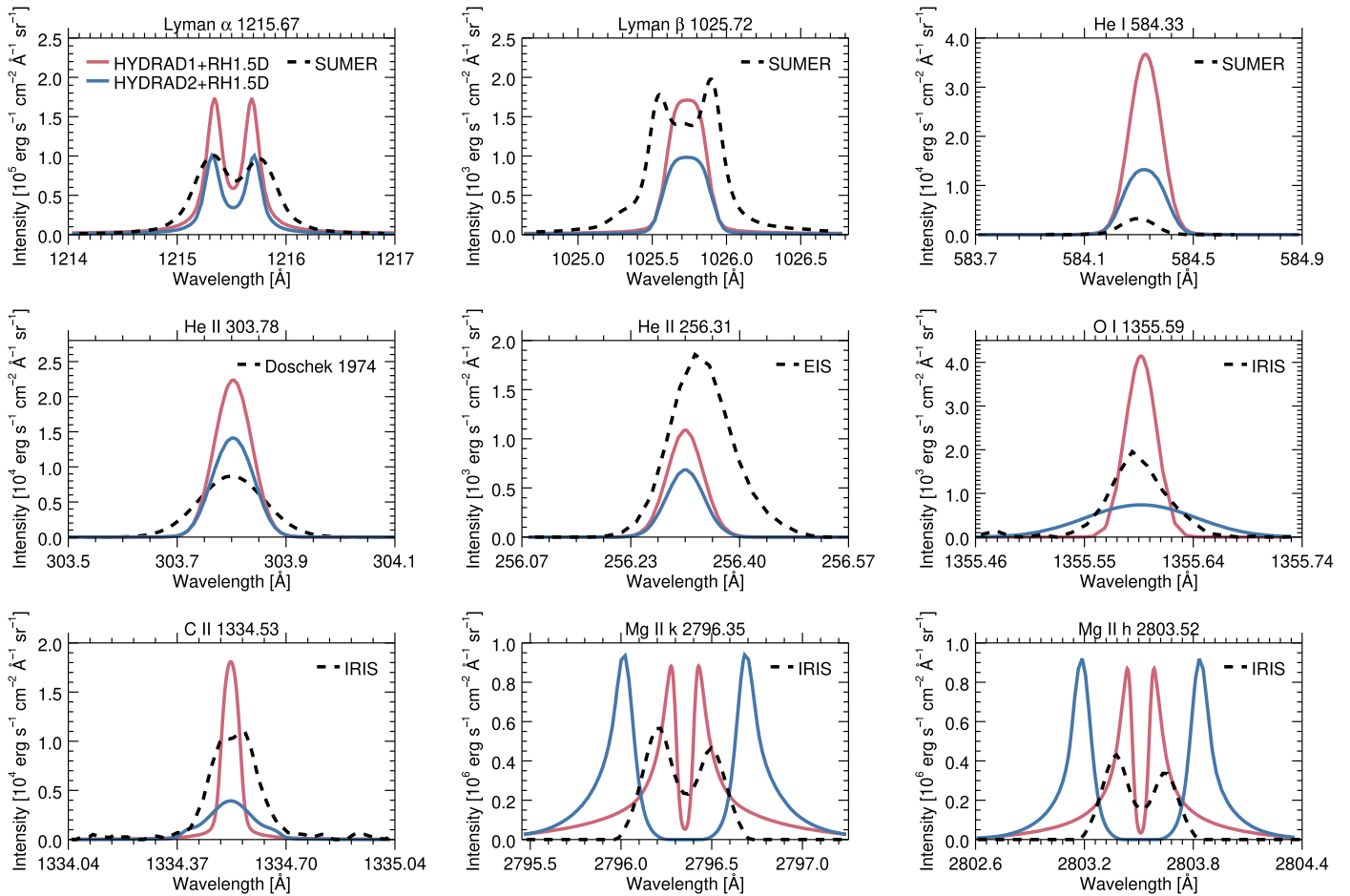


**Figure 13.** Comparison of the line profiles synthesized with RH1.5D using two density profiles against quiet Sun observations from SUMER, the rocket flight reported in Doschek et al. (1974), EIS, and *IRIS*, as labeled. From left to right, top to bottom: Ly $\alpha$ , Ly $\beta$ , He I 584 Å, He I 304 Å, He II 256 Å, O I 1355.6 Å, C II 1334.4 Å, Mg II k 2796.4 Å, and Mg II h 2803.5 Å. The lines show varying degrees of agreement, but it is clear that not all of the lines can be reproduced simultaneously.

X-ray light curves (Reeves & Warren 2002; Warren & Doschek 2005; Warren 2006; Reep & Toriumi 2017), late-phase heating (Reeves et al. 2007; Qiu & Longcope 2016; Zhu et al. 2018), or spectral-line considerations (Kowalski et al. 2017a; Rubio da Costa & Kleint 2017). Interestingly, despite tremendous advances in spatial resolution, there are still indications that the basic flaring loop is unresolved. For example, the long-lasting redshifts in Si IV seen by *IRIS* during many flares can be explained by multithreaded modeling (Reep et al. 2016b), but only if there are more than 60 loops rooted within a single pixel, suggesting that the observations do not come anywhere near resolving the basic filamentation of flares.

In order to tackle both of these computational challenges, we have implemented an approximation to the radiative transfer equations into HYDRAD that gives a fast and reasonable solution to the level populations of hydrogen using a six-level atom. In turn, we have improved the calculation of the electron density across the chromosphere and the corona, which more precisely determines radiative losses and dynamic processes such as evaporation speeds. The code is computationally light enough that many simulations of loops with a wide parameter space can be run in a modest amount of time, which is particularly important for multithreaded modeling. Furthermore, the code has been parallelized with good scaling up to at

least 32 cores, offsetting the loss in computational time due to the NLTE calculations.

In order to test this model, we have developed a multi-threaded model of a flaring event seen by *IRIS*. In the observations, it was found that O I remained approximately stationary, Si IV and C II showed long-lasting redshifts that persisted for more than 60 minutes, and while Mg II formed redshifted, its velocity gradually slowed (Warren et al. 2016). A multithreaded model was able to reproduce Si IV closely, both in terms of intensity and Doppler shifts, but faltered with C II and O I (Reep et al. 2016b). In this paper, we revisited those simulations with the improved chromospheric model and the RH1.5D code, recalculating these lines along with Mg II and finding fair agreement. The O I was found to be approximately stationary, C II was strongly redshifted for long periods of time, and Mg II forms were redshifted with a gradually decaying speed. The absolute intensities could be reproduced in either O I or C II, but not both simultaneously, with this model. These results confirm the importance of NLTE effects on the formation of these lines, even in a multithreaded model, but they do not settle all of the issues.

A close examination of the initial atmosphere reveals that there is, in general, poor agreement with observations of the quiet Sun and preflare observations. The assumption of either a VAL C or FAL C model does not reproduce all chromospheric

**Table 2**

The Integrated Intensities of Each Line, Calculated for Each Case in Figure 13, as well as for the FAL C Atmosphere (Fontenla et al. 1993)

Line, $\lambda_0$	Source	$\int I_\lambda d\lambda$	Ratio
Å		erg s <sup>-1</sup> cm <sup>-2</sup> sr <sup>-1</sup>	
Ly $\alpha$ 1215.67	SUMER	$8.51 \times 10^4$	1.00
	FAL C	$3.89 \times 10^4$	0.45
	HYDRAD 1	$8.33 \times 10^4$	0.98
	HYDRAD 2	$4.89 \times 10^4$	0.57
Ly $\beta$ 1025.72	SUMER	$1.07 \times 10^3$	1.00
	FAL C	$4.09 \times 10^2$	0.38
	HYDRAD 1	$5.55 \times 10^2$	0.52
	HYDRAD 2	$3.52 \times 10^2$	0.33
He I 584.33	SUMER	$5.02 \times 10^2$	1.00
	FAL C	$3.41 \times 10^2$	0.68
	HYDRAD 1	$5.32 \times 10^3$	10.60
	HYDRAD 2	$3.52 \times 10^3$	7.01
He II 303.78	Doschek et al.	$1.31 \times 10^3$	1.00
	FAL C	$8.92 \times 10^2$	0.68
	HYDRAD 1	$1.89 \times 10^3$	1.44
	HYDRAD 2	$1.31 \times 10^3$	1.00
He II 256.31	EIS	$2.16 \times 10^2$	1.00
	FAL C	$3.47 \times 10^1$	0.16
	HYDRAD 1	$7.48 \times 10^1$	0.35
	HYDRAD 2	$4.86 \times 10^1$	0.22
O I 1355.598	<i>IRIS</i>	$1.11 \times 10^2$	1.00
	FAL C	$3.14 \times 10^1$	0.28
	HYDRAD 1	$1.36 \times 10^2$	1.23
	HYDRAD 2	$8.53 \times 10^1$	0.77
C II 1334.535	<i>IRIS</i>	$2.10 \times 10^3$	1.00
	FAL C	$2.14 \times 10^2$	0.10
	HYDRAD 1	$1.28 \times 10^3$	0.61
	HYDRAD 2	$7.10 \times 10^2$	0.34
Mg II k 2796.35	<i>IRIS</i>	$2.13 \times 10^5$	1.00
	FAL C	$1.54 \times 10^5$	0.72
	HYDRAD 1	$3.31 \times 10^5$	1.55
	HYDRAD 2	$3.89 \times 10^5$	1.83
Mg II h 2803.52	<i>IRIS</i>	$1.41 \times 10^5$	1.00
	FAL C	$1.13 \times 10^5$	0.80
	HYDRAD 1	$2.71 \times 10^5$	1.92
	HYDRAD 2	$3.18 \times 10^5$	2.26

**Note.** The final column shows the ratio of the integrated intensity to that observed.

lines simultaneously and likely requires modification. Unfortunately, simply scaling the density and assumed microturbulence to better match any individual observed line does not necessarily improve the correspondence of other lines with observations. It is likely that it is also necessary to alter the shape of the temperature profile to improve the fit. Further, it is implausible that multiple events are described by the same initial atmosphere, and in general, we should not assume the same atmospheric profile for all events. We therefore suggest that preflare atmospheres used in simulations be fine-tuned to preflare observations of events under study (e.g., Reep et al. 2016a), and that future instrumentation (e.g., DKIST or Solar-C), combined with spectral inversion methods (Socas-Navarro et al. 2000), can assist in that endeavor. We plan a future study to address the importance and plausibility of such a method.

J.W.R. was supported by a Jerome and Isabella Karle Fellowship for this work. This work was supported by NASA’s *Hinode* project. *Hinode* is a Japanese mission developed and launched by ISAS/JAXA, with NAOJ as domestic partner and NASA and STFC (UK) as international partners. It is operated by these agencies in cooperation with ESA and NSC (Norway). S.J.B. acknowledges the support of NASA by grant NNX17AD31G during this work. The numerical simulations were performed under a grant of computer time from the Department of Defense High Performance Computing Program. The authors would like to thank the anonymous referee for providing many helpful comments that significantly improved the model. The authors would like to thank Drs. Tiago Pereira, Han Uitenbroek, Mats Carlsson, Jorrit Leenaarts, Joel Allred, Graham Kerr, and Jaroslav Dudík for addressing many questions that we had while working on various stages of this paper. We would like to thank Sam Cable for his efforts in parallelizing HYDRAD. This research has made use of NASA’s Astrophysics Data System. *IRIS* is a NASA small explorer mission developed and operated by LMSAL with mission operations executed at NASA Ames Research Center and major contributions to downlink communications funded by ESA and the Norwegian Space Centre. We have made use of color-blind safe color tables where possible, using the IDL routine “distinct\_colors” by Paul Tol (<https://personal.sron.nl/~pault/>). The research leading to these results has received funding from the European Community’s Seventh Framework Programme (FP7/2007–2013) under grant agreement No. 606862 (F-CHROMA) and from the Research Council of Norway through the Programme for Supercomputing.

## Appendix

### A.1. RADYN Comparison

In this appendix, we briefly compare the method of approximating level populations against the commonly used RADYN model. We do not enumerate all of the differences in physics and numerics here, though it would be a useful exercise to show a comparison of all the strengths and weaknesses of commonly used models such as these two. Our primary purpose here is to compare the chromospheric electron density that results from the Sollum method compared to a treatment that solves the full radiative transfer equation.

We show two simulations of electron beam heating, taken from the F-CHROMA website,<sup>6</sup> model numbers 078 and 012, which had electron beams with low-energy cutoff  $E_c = 10$  keV, spectral index  $\delta = 8$ , and peak energy flux  $F_0 = 3 \times 10^9$  and  $3 \times 10^{10}$  erg s<sup>-1</sup> cm<sup>-2</sup>, heated with a triangular profile over 20 s. The loop length is 22 Mm in total (11 Mm in RADYN, which only solves half the loop), and the simulations were run for 50 s. We copied RADYN’s chromospheric temperature profile into HYDRAD, set the footpoint density to agree with RADYN, and then allowed HYDRAD to solve for the hydrostatic initial conditions. Because the two codes have different assumed background heating functions and radiative loss functions, the initial conditions do not agree perfectly but are fairly close at all heights. Nonequilibrium ionization was used only for helium and calcium in HYDRAD for this comparison, as RADYN solves these in nonequilibrium as well.

<sup>6</sup> <https://star.pst.qub.ac.uk/wiki/doku.php/public/solarmodels/start>

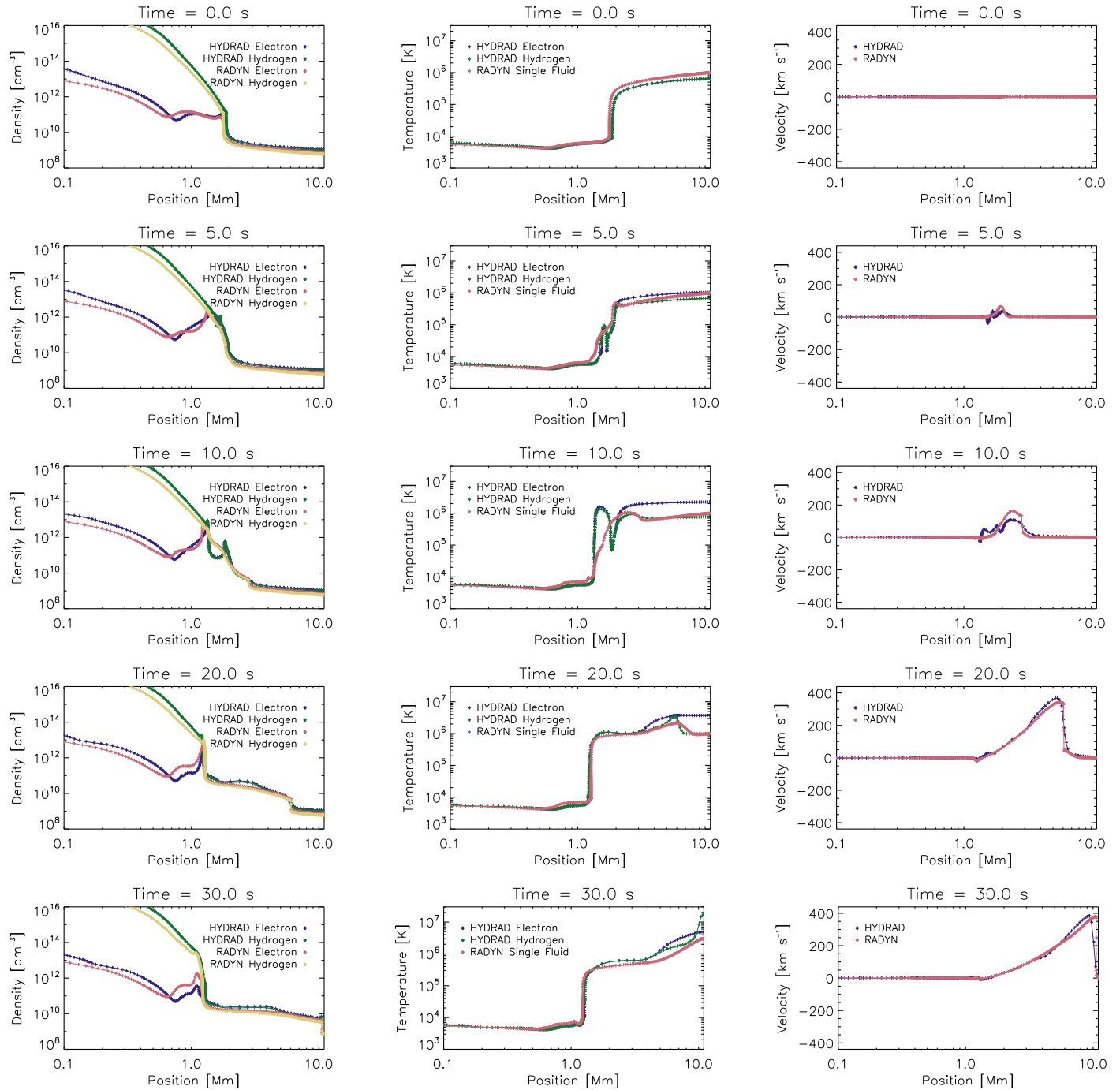


**Figure 14.** Comparison between HYDRAD and RADYN using model 078 from the F-CHROMA website. From the left, we show the densities, temperatures, and bulk velocities in the simulations at selected times. We find excellent agreement between the two, in general, though there are differences. An animation of the comparison between HYDRAD and RADYN is available in the electronic version of this paper. The animation includes the full duration of the simulation at 0.1 s cadence. The left panels of the animation show the simulated densities, temperatures, and bulk velocities, while the right panels show the evolution of the hydrogen level populations.

(An animation of this figure is available.)

In Figure 14, we show the comparison of the weaker case, model 078 at times 0, 5, 10, 20, and 30 s into the simulation. In the online version, we have provided movies of the comparisons that show all time steps from 0 to 50 s at 0.1 s cadence, along with a movie comparing the hydrogen level populations. The left column shows the electron and hydrogen densities along the loop. Due to the differences in the initial conditions, HYDRAD is slightly denser in the chromosphere,

particularly near the photosphere. The electron density evolution shows good agreement until the cooling period, when HYDRAD's chromosphere cools more quickly than RADYN's, so that its ionized fraction falls more rapidly. The middle column shows the temperatures along the loop. RADYN's temperature (single fluid) is found to be closer to HYDRAD's hydrogen temperature in its temporal and spatial evolution than to the electron temperature. Finally, the right



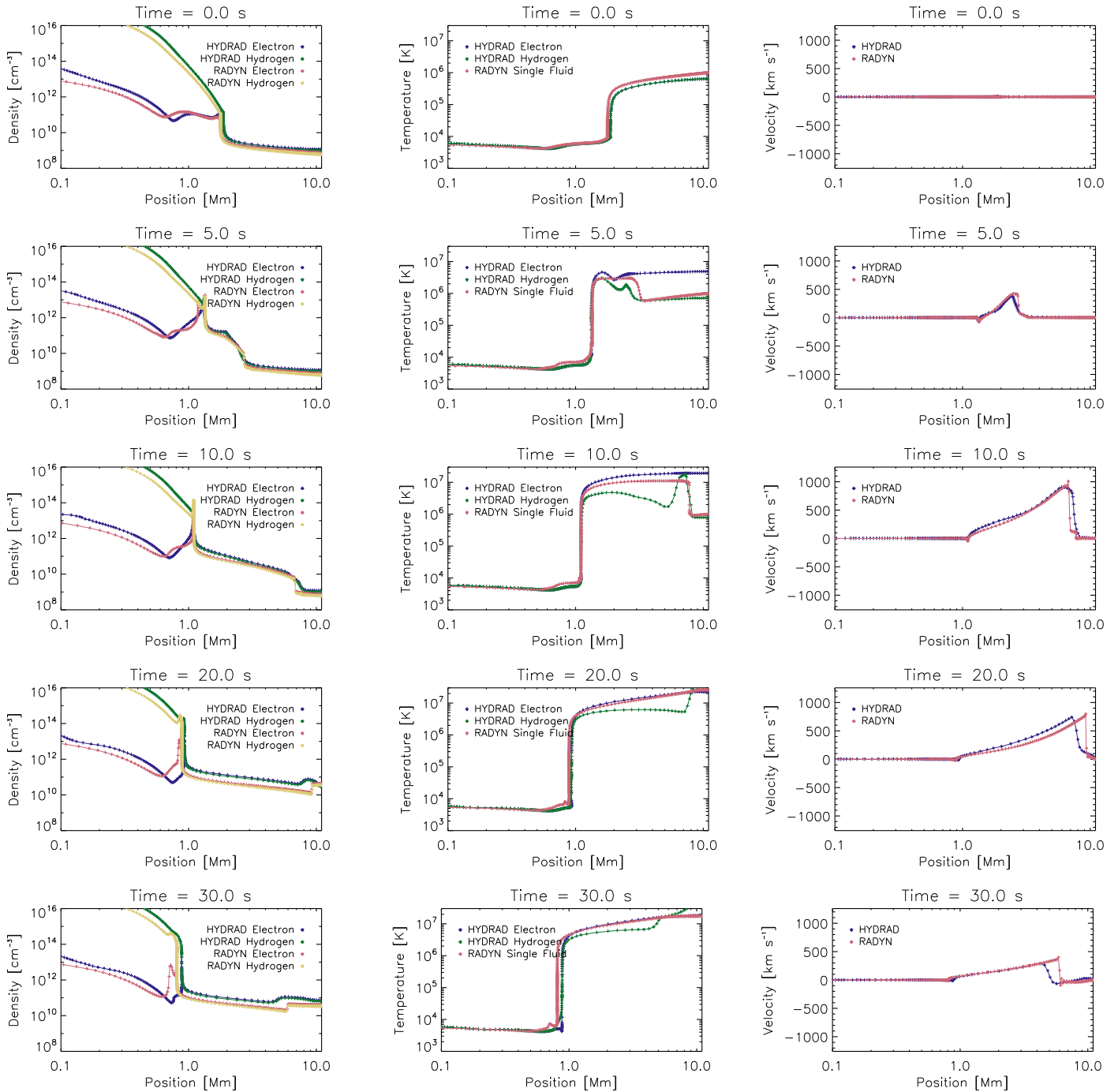


**Figure 15.** Similar to the previous figure, using model 012 from the F-CHROMA website, which has a beam-heating rate 10 times stronger than model 078. Once again, despite significant differences in numerics and physics, the two compare well in general. An animation of the model comparisons is available in the electronic version of this paper. The animation includes the full duration of the simulation at 0.1 s cadence. The left panels of the animation show the simulated densities, temperatures, and bulk velocities, while the right panels show the evolution of the hydrogen level populations.

(An animation of this figure is available.)

column shows the bulk velocity in the two codes, which agrees closely at all times. Considering the significant differences in physics and numerics between the codes, we consider the overall agreement to be excellent.

In Figure 15, we show a comparison to model 012 from the F-CHROMA website, which has an electron beam with the same cutoff and spectral index but an energy flux 10 times higher than the previous case. We find similar agreement: the overall evolution is comparable, but the details differ because

of differences in both the physics and numerics. In particular, following the cessation of heating, we once again find that the chromospheric electron density falls more rapidly in HYDRAD than RADYN but is otherwise comparable.

#### ORCID iDs

Jeffrey W. Reep  <https://orcid.org/0000-0003-4739-1152>  
 Harry P. Warren  <https://orcid.org/0000-0001-6102-6851>

## References

- Allred, J. C., Kowalski, A. F., & Carlsson, M. 2015, *ApJ*, **809**, 104
- Antolin, P., Vissers, G., Pereira, T. M. D., Rouppe van der Voort, L., & Scullion, E. 2015, *ApJ*, **806**, 81
- Bradshaw, S. J., & Cargill, P. J. 2013, *ApJ*, **770**, 12
- Bradshaw, S. J., & Mason, H. E. 2003a, *A&A*, **401**, 699
- Bradshaw, S. J., & Mason, H. E. 2003b, *A&A*, **407**, 1127
- Brooks, D. H., Warren, H. P., Ugarte-Urra, I., & Winebarger, A. R. 2013, *ApJL*, **772**, L19
- Brosius, J. W., & Inglis, A. R. 2017, *ApJ*, **848**, 39
- Brosius, J. W., & Phillips, K. J. H. 2004, *ApJ*, **613**, 580
- Carlsson, M., & Leenaarts, J. 2012, *A&A*, **539**, A39
- Carlsson, M., & Stein, R. F. 1992, *ApJL*, **397**, L59
- Carlsson, M., & Stein, R. F. 2002, *ApJ*, **572**, 626
- De Pontieu, B., Title, A. M., Lemen, J. R., et al. 2014, *SoPh*, **289**, 2733
- Del Zanna, G., Dere, K. P., Young, P. R., Landi, E., & Mason, H. E. 2015, *A&A*, **582**, A56
- Doschek, G. A., Behring, W. E., & Feldman, U. 1974, *ApJL*, **190**, L141
- Dudík, J., Polito, V., Džifčáková, E., Del Zanna, G., & Testa, P. 2017, *ApJ*, **842**, 19
- Emslie, A. G. 1978, *ApJ*, **224**, 241
- Fang, C., Henoux, J. C., & Gan, W. Q. 1993, *A&A*, **274**, 917
- Fang, C., Xu, Z., & Ding, M. D. 2003, *JKAS*, **36**, S55
- Fisher, G. H. 1989, *ApJ*, **346**, 1019
- Fontenla, J. M., Avrett, E. H., & Loeser, R. 1993, *ApJ*, **406**, 319
- Graham, D. R., & Cauzzi, G. 2015, *ApJL*, **807**, L22
- Gudiksen, B. V., Carlsson, M., Hansteen, V. H., et al. 2011, *A&A*, **531**, A154
- Heinzel, P., Kašparová, J., Varady, M., Karlický, M., & Moravec, Z. 2016, in IAU Symp. 320, *Solar and Stellar Flares and their Effects on Planets*, ed. A. G. Kosovichev, S. L. Hawley, & P. Heinzel, **233**
- Hori, K., Yokoyama, T., Kosugi, T., & Shibata, K. 1997, *ApJ*, **489**, 426
- Hori, K., Yokoyama, T., Kosugi, T., & Shibata, K. 1998, *ApJ*, **500**, 492
- Ishikawa, R., Uitenbroek, H., Goto, M., Iida, Y., & Tsuneta, S. 2018, *SoPh*, **293**, 74
- Ishikawa, S.-n., Kubo, M., Katsukawa, Y., et al. 2017, *ApJ*, **846**, 127
- Johnson, L. C. 1972, *ApJ*, **174**, 227
- Judge, P. G. 2017, *ApJ*, **851**, 5
- Kašparová, J., Varady, M., Heinzel, P., Karlický, M., & Moravec, Z. 2009, *A&A*, **499**, 923
- Kowalski, A. F., Allred, J. C., Daw, A., Cauzzi, G., & Carlsson, M. 2017a, *ApJ*, **836**, 12
- Kowalski, A. F., Allred, J. C., Uitenbroek, H., et al. 2017b, *ApJ*, **837**, 125
- Kuridze, D., Mathioudakis, M., Simões, P. J. A., et al. 2015, *ApJ*, **813**, 125
- Lee, K.-S., Imada, S., Watanabe, K., Bamba, Y., & Brooks, D. H. 2017, *ApJ*, **836**, 150
- Leenaarts, J., Carlsson, M., Hansteen, V., & Rutten, R. J. 2007, *A&A*, **473**, 625
- Leenaarts, J., Pereira, T., & Uitenbroek, H. 2012, *A&A*, **543**, A109
- Leenaarts, J., Pereira, T. M. D., Carlsson, M., Uitenbroek, H., & De Pontieu, B. 2013, *ApJ*, **772**, 89
- Leenaarts, J., & Wedemeyer-Böhm, S. 2006, *A&A*, **460**, 301
- Li, D., Ning, Z. J., & Zhang, Q. M. 2015, *ApJ*, **813**, 59
- Lin, H.-H., & Carlsson, M. 2015, *ApJ*, **813**, 34
- Pereira, T. M. D., & Uitenbroek, H. 2015, *A&A*, **574**, A3
- Polito, V., Reep, J. W., Reeves, K. K., et al. 2016, *ApJ*, **816**, 89
- Press, W. H., Teukolsky, S. A., Vetterling, W. T., & Flannery, B. P. 2002, in *Numerical Recipes in C++: The Art of Scientific Computing* (Cambridge: Cambridge University Press)
- Qiu, J., & Longcope, D. W. 2016, *ApJ*, **820**, 14
- Rathore, B., & Carlsson, M. 2015, *ApJ*, **811**, 80
- Reep, J. W., Bradshaw, S. J., & Holman, G. D. 2016a, *ApJ*, **818**, 44
- Reep, J. W., Bradshaw, S. J., & McAteer, R. T. J. 2013, *ApJ*, **778**, 76
- Reep, J. W., Polito, V., Warren, H. P., & Crump, N. A. 2018, *ApJ*, **856**, 149
- Reep, J. W., & Toriumi, S. 2017, *ApJ*, **851**, 4
- Reep, J. W., Warren, H. P., Crump, N. A., & Simões, P. J. A. 2016b, *ApJ*, **827**, 145
- Reeves, K. K., & Warren, H. P. 2002, *ApJ*, **578**, 590
- Reeves, K. K., Warren, H. P., & Forbes, T. G. 2007, *ApJ*, **668**, 1210
- Rubio da Costa, F., & Kleint, L. 2017, *ApJ*, **842**, 82
- Rubio da Costa, F., Kleint, L., Petrosian, V., Sainz Dalda, A., & Liu, W. 2015, *ApJ*, **804**, 56
- Rybicki, G. B., & Hummer, D. G. 1991, *A&A*, **245**, 171
- Scharmer, G. B. 1981, *ApJ*, **249**, 720
- Scharmer, G. B., & Carlsson, M. 1985, *JCoPh*, **59**, 56
- Socas-Navarro, H., Ruiz Cobo, B., & Trujillo Bueno, J. 1998, *ApJ*, **507**, 470
- Socas-Navarro, H., Trujillo Bueno, J., & Ruiz Cobo, B. 2000, *ApJ*, **530**, 977
- Sollum, E. 1999, Master's thesis, Univ. Oslo
- Tian, H., & Chen, N. H. 2018, *ApJ*, **856**, 34
- Uitenbroek, H. 2001, *ApJ*, **557**, 389
- Vernazza, J. E., Avrett, E. H., & Loeser, R. 1981, *ApJS*, **45**, 635
- Warren, H. P. 2006, *ApJ*, **637**, 522
- Warren, H. P., & Doschek, G. A. 2005, *ApJL*, **618**, L157
- Warren, H. P., Reep, J. W., Crump, N. A., & Simões, P. J. A. 2016, *ApJ*, **829**, 35
- Wiese, W. L., & Fuhr, J. R. 2009, *JPCRD*, **38**, 565
- Zhu, C., Qiu, J., & Longcope, D. W. 2018, *ApJ*, **856**, 27